Hochschule für Angewandte Wissenschaften Hamburg

Fakultät Life Sciences

Implementation and evaluation of a radial spin echo sequence for diffusion tensor imaging (RAISED) pulse sequence for diffusion tensor imaging (DTI) of articular cartilage *in vivo* at 3 T

Master Thesis

Biomedical Engineering

Presented by

Eike Susann Dettmann

1846399

HAW Bergedorf, Hamburg

May 2013

Supervisor: Prof. Dr. Friedrich Ueberle HAW Hamburg

Supervisor: Dr. José G. Raya NYU Langone Medical Center

Acknowledgement

First and foremost, my utmost gratitude goes to my supervisor José Raya for giving me the opportunity to come to New York and be part of such a great team. His constant support and patience made my time in New York a wonderful experience. I can't say thank you enough for his tremendous support and help. Without his guidance and consistent help this thesis would not have been possible. I would also like to thank all my colleagues at the CBI who made coming to work every day so enjoyable. I am very grateful to Prof. Dr. Friedrich Ueberle for the supervision of my thesis. I would also like to express my deepest appreciation to my family who has supported me throughout the entire process. They have always believed in me and my goals and I could have not done this without them. Last but not least I would like to thank my closest friends for always being there for me, even during my time far away in New York.

Abstract

Osteoarthritis (OA) is a degenerative painful disease of the joint which functionally limits the affected joint. It is the major cause of chronic disabilities in industrialized countries. The absence of a robust and non-invasive way to detect the progression of the disease makes it difficult to find new and effective therapies and drugs. Thus finding a non-invasive way to detect OA in its early stages is of high importance.

Articular cartilage is one of the first tissues to suffer changes in the progression of OA with the decay of two components of the extracellular matrix, proteoglycan (PG) and collagen. Many researchers have focused on monitoring the decay of these two components with available parameters, such as T_2 or $T_{1\rho}$ [1, 2]. Diffusion Tensor Imaging (DTI) is the only MRI method that offers the advantage of being sensitive to both PG and collagen and is therefore a promising approach to evaluate the integrity of the cartilage extracellular matrix [3-5].

Although the use of DTI is promising, its acquisition *in vivo* is challenging. Many standard diffusion sequences, such as diffusion-weighted echo planar imaging (DW-EPI) are useless [6-8]. At 7 T a working protocol for imaging articular cartilage has been successfully implemented by Raya *et al.* using a line scan diffusion sequence [9]. However, 7 T scanners are not approved in clinical environments. Hence, it needs to be applicable on 3 T scanners as well.

The aim of this Master's thesis is to provide DTI with high resolution images at 3 T by implementing and evaluating an in house written radial spin echo sequence for diffusion tensor imaging (RAISED) for DTI of articular cartilage in the knee. This is achieved in four steps.

1. *Implementation of the RAISED sequence at 3 T*
2. *Optimization of the protocol:* The protocol was theoretically optimized to obtain images with sufficient signal-to-noise ratio (SNR)
3. *Ex vivo validation of the RAISED sequence: Ex vivo* validation was performed on water and asparagus phantoms
4. *In vivo application in healthy and OA subjects:* Images of healthy and OA subjects were acquired with the RAISED sequence. Diffusion parameters were calculated and evaluated. Statistical analysis was performed to determine whether significant differences were present between the healthy control subjects and the OA subjects.

Zusammenfassung

Arthrose (OA) ist eine degenerative, schmerzhafte und funktionell einschränkende Erkrankung des Gelenks. Es ist eine der häufigsten chronischen Erkrankungen in Industrieländern. Sie führt zu erheblichen individuellen Beeinträchtigungen der Patienten und stellt eine große sozioökomische Belastung dar. Sowohl effektive Behandlungsmethoden als auch eine robuste und nichtinvasive Methode zur Beurteilung des Krankheitsverlaufs existieren nicht. Aus diesem Grund ist die Entwicklung einer neuen nichtinvasiven Methode zur frühen Erkennung von OA von großer Bedeutung.

Der Gelenkknorpel ist mit dem Abbau von Proteoglykanen (PG) und Kollagen eins der ersten Gewebe in dem bei Arthrose Veränderungen stattfinden. Die Beurteilung dieser Veränderungen, mit Hilfe von MR-Parametern wie T_2 oder $T_{1\rho}$, war der Fokus vieler Forschungsarbeiten. Diffusions-Tensor-Bildgebung (DTI) ist als einzige MR-Methode sensitiv auf den Abbau von PG und Kollagen und somit sehr vielversprechend [3-5].

Obwohl DTI in der Bildgebung vom Gelenkknorpel aussichtsreich zu sein scheint, stellt die *in vivo* Anwendung eine Herausforderung dar. Viele gängige Methoden, wie die diffusionsgewichtete Echo-Planar-Bildgebung (DW-EPI), sind unbrauchbar [6-8]. Raya *et al.* setzten ein Protokoll mit exzellenter Bildqualität mit Hilfe einer diffusionsgewichteten Line-Scan Sequenz an einem 7 T Ganzkörper Scanner auf [9]. Allerdings sind 7 T Geräte im klinischen Bereich nicht zugelassen, weshalb das Aufsetzen eines erfolgreichen Protokolls an einem 3 T Scanner notwendig ist.

Ziel dieser Masterarbeit ist es, mit der Implementierung und Evaluierung von einer hauseigenen radialen Spin-Echo Sequenz für die Diffusions-Tensor-Bildgebung (RAISED) für DTI von Gelenkknorpel im Knie DTI mit hochauflösenden Bildern an 3 T zu erhalten. Erreicht wird dieses in vier Schritten.

1. *Implementierung der RAISED Sequenz an 3 T*
2. *Optimierung des Protokolls:* Das Protokoll wurde theoretisch optimiert, um Bilder mit ausreichendem Signal-Rausch-Verhältnis (SNR) zu erhalten.
3. *Ex vivo Validierung der RAISED Sequenz: Ex vivo* Validierung wurde an Wasser- und Spargel-Phantomen durchgeführt
4. *In vivo Anwendung an gesunden und OA Subjekten:* Diffusions-Parameter wurden für die gesunden und an OA erkrankten Subjekte gemessen, berechnet und verglichen.

Table of Contents

Figures

Tables

Abbreviations

ACR	The American College of Rheumatology
ADC	Apparent Diffusion Coefficient
dGEMRIC	Delayed Gadolinium Enhanced MRI of Cartilage
DTI	Diffusion Tensor Imaging
DWI	Diffusion-Weighted Imaging
DW-EPI	Diffusion-Weighted Echo Planar Imaging
DW-HASTE	Diffusion-Weighted Half Fourier Acquisition Single Shot Turbo Spin Echo
FA	Fractional Anisotropy
FOV	Field of View
GAG	Glycosaminoglycan
ISMRM	The International Society for Magnetic Resonance in Medicine
MD	Mean Diffusivity
MRI	Magnetic Resonance Imaging
OA	Osteoarthritis
OARSI	Osteoarthritis Research Society International
PG	Proteoglycan
RAISED	Radial Spin Echo Diffusion Sequence
RF	Radio Frequency
RO	Readout
SAR	Specific Absorption Rate
SEM	Scanning Electron Microscopy
SNR	Signal to Noise Ratio
TV	Total Variation
WVF	Water Volume Fraction

1. Introduction

Osteoarthritis (OA) is a degenerative disease of the joint. It is painful and functionally limits the affected joint. OA is accompanied by progressive loss of articular cartilage, eburnation of subchondral bone and inflammation of the joint capsule. OA is the major cause of chronic disabilities in industrialized countries and as a result of the high prevalence and the absence of effective therapies it is a big socioeconomic burden. Finding new therapies and drugs has been proven to be very difficult because a robust and non-invasive way to detect the progression of the joint disease is non-existent. Hence, it would be of high importance to find such a non-invasive method to detect osteoarthritis in its early stages.

The articular cartilage is one of the first tissues to suffer changes in progression of OA. There are two components in the cartilage which decay when OA is present, the macromolecules protoeoglycan (PG) and collagen. Hence, articular cartilage is seen as an important factor in the diagnostics of OA and has been the focus of many researchers during the last few decades. However, monitoring the decay of these two components with the available parameters, such as T_2, $T_{1\rho}$ and sodium, has been proven to be difficult. Diffusion Tensor Imaging (DTI) offers the advantage of being sensitive to both components and is therefore a promising approach to evaluate the integrity of the cartilage extracellular matrix [3-5].

The most commonly used sequence for diffusion studies on articular cartilage is the single-shot diffusion sequence diffusion-weighted echo planar imaging (DW-EPI). While the acquisition time is kept short and motion during the acquisition is thus prevented, DW-EPI results in image distortions and low resolution [6-8], which is critical for cartilage as it is only 3-5 mm thick.

Therefore, due to the low T_2 of cartilage and the need of high resolution images, a sequence is needed which is useful for imaging articular cartilage by providing high quality images. Raya *et al.* have successfully implemented a working protocol for imaging articular cartilage at 7 T using a line scan diffusion sequence [9]. Nevertheless, 7 T scanners are not approved for clinical imaging. Hence, in order to introduce this method to clinical environments, the DTI technique has to be successful for 3 T as well to guarantee accurate measurement of the diffusion parameters.

This Master thesis is based on the implementation and evaluation of an in house written radial spin echo sequence for diffusion tensor imaging (RAISED) for DTI of articular cartilage in the knee at 3 T. This objective is achieved in four steps:

1. Implementation of the RAISED sequence
2. Optimization of the protocol
3. *Ex vivo* validation of the RAISED sequence
4. *In vivo* application in healthy and OA subjects

In chapter 2 I summarize the different components of articular cartilage and their properties before describing the changes in articular cartilage during osteoarthritis. The current methods of MR imaging of articular cartilage are then reviewed in chapter 3 which is followed by a description of radial sequences and their importance for DTI in chapter 4. The calibration and optimization of the radial sequence is the subject of chapters 5 and 6 and finally the *in vivo* validation is shown and discussed in chapter 7. I conclude with a summary of the research and outlook on future applications.

2. Anatomy and physiology of articular cartilage

2.1 Anatomy

Hyaline cartilage is a connective tissue that is present in many joint surfaces, *e.g.* contact surfaces of bones in joints are covered by a layer of cartilage. It is also present in the larynx, between the ribs and the sternum and in the nose. Articular cartilage does not have blood vessels and nerves. Hence, it gets its nutrition only by diffusion [10]. In healthy state it is translucent bluish white in color and possesses stiff mechanical properties. The cartilage reduces the friction between the joints, distributes the load to the boney ends and absorbs the mechanical shock.

The knee is the biggest and most complex joint in the human body and the focus of this thesis. It consists of three elements, the femur, the tibia and the patella (Fig. 1). The knee joint has to bear high strains. Hence, the rather thick cartilage of the knee is subject to high mechanical loading and thus commonly affected by OA.

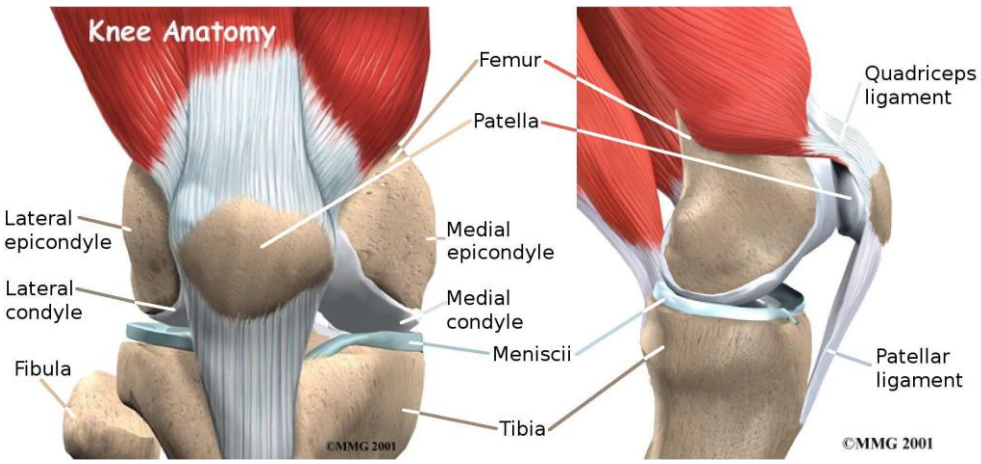

Figure 1: Anatomy of the knee joint [11]

2.1.1 Composition

Articular cartilage is composed of several different materials, a matrix which predominately consists of proteoglycans (PG) and collagen and other ionic components, such as Na^+. Chondrocytes, the only cellular components, are of single-cell type and responsible for the synthesis and degradation of all macromolecules in the extracellular matrix and thus for maintaining a steady-state equilibrium [10]. Sorted by their percentage of the wet weight of the cartilage, the different elements of the cartilage are as follows:

Water: Water is the main component of articular cartilage, taking up 60 to 80% of its wet weight. The water content in cartilage decreases with age. Furthermore, water is unevenly spread throughout the cartilage. The highest amount of water is found at the articular surface and decreases towards the bone-cartilage interface. With joint compression, the water moves in and out of the cartilage matrix and thus ensures that nutrients reach the chondrocytes [10, 12-14].

MRI is commonly based on the detection of ^{1}H. It is mostly bound to the water molecules. Hence, the water volume fraction (WVF) can be detected with MRI. The WVF decreases from the articular surface to the bone-cartilage interface in healthy patellar cartilage [15]. Raya *et al.* showed that WVF increases with the grade of OA. In healthy cartilage the average WVF was (74±5)%, (77±5)% in moderate OA and (80±5)% in severe OA [15]. In Fig. 2 the WVF map of a healthy cartilage sample is illustrated.

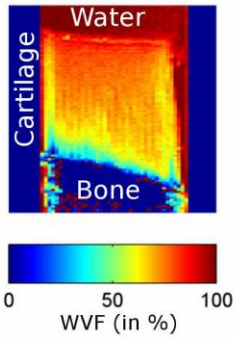

Figure 2: WVF map of healthy patellar cartilage (adapted from [15])

Collagen: Collagen makes up about 10 to 30% of the articular cartilage [14]. Like water, it also decreases with age and is unevenly distributed in cartilage [13, 16]. The highest amount of collagen is present at the articular surface and decreases towards the bone-cartilage interface [10, 12, 13, 16]. Collagen appears as fibrils with thick and thin diameters of approximately 30 nm and 100 nm [16-20].

Proteoglycans: Proteoglycans (PGs) are responsible for 3 to 10% of the cartilage [14]. A proteoglycan consists of a central core protein to which 100 to 150 glycosaminogycan (GAG) side chains are attached covalently through a link protein [21-23].The most common proteoglycan in cartilage is aggrecan. Due to the sulfate and carboxyl residues of the GAG side chains, the PGs are negatively charged and thus attract cations, such as Na^{+}, and water molecules, hence they are expanding in volume. PG forces the water out of the matrix and

lets it back in when a force is exerted on the cartilage and is therefore an important aspect for the capability of cartilage to resist compression [10].

Chondrocytes: The chondrocytes take up about 1% of the cartilage volume and are the only cellular component. They are found in small chambers called lacunae. Chondrocytes are responsible for the synthesis and degradation of all macromolecules in the extracellular matrix and the composition of the matrix [10, 24]. They vary in shape, size, orientation and metabolic activity [25, 26], but they all have the organelles that are needed to synthesize the matrix components.

The interaction of the extracellular matrix with the chondrocytes is responsible for the balance between the synthetic and degradative activities of the chondrocytes. If the matrix is deformed, a variety of signals is produced, *e.g.* mechanical or electrical signals. These signals can be detected by chondrocytes which react to them with the release or inhibition of cytokines. These on the other hand are responsible for enhancing or retarding the synthesis or degradation of the matrix [27-29]. In healthy subjects, the chondrocytes keep a low rate of replacement of the cartilage matrix with a half-life of collagen over 100 years [30] and a half-life of PG in the range of 3 to 24 years [31].

Other components: There are also several other components present in articular cartilage. Their volume fractions are below 1% of the wet weight, such as free cations (mainly ^{23}Na) which are responsible for maintaining the electro neutrality of the extracellular matrix.

In addition the articular cartilage contains several non-collagenous proteins. Most of these proteins bind the different components of the extracellular matrix [32].

2.1.2 Structure

With the help of scanning electron microscopy (SEM), it was observed that the articular cartilage consists of four well differentiated zones with respect to the orientation of the collagen fibrils (Fig. 3), the tangential, the transitional, the radial and the calcified zone [10, 17].

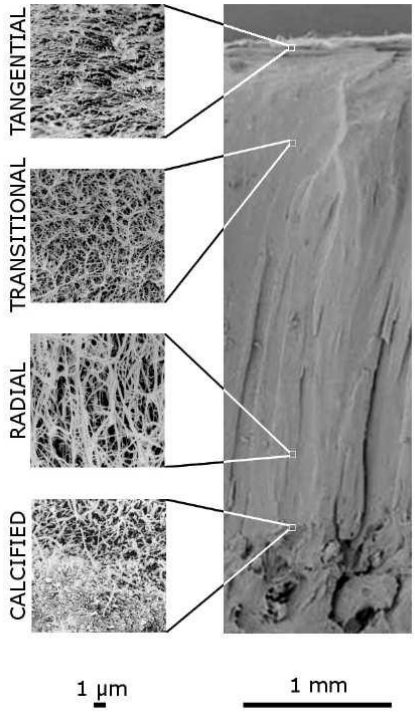

Figure 3: High resolution SEM images of the different zones in the articular cartilage (adapted from[33])

The borders between the first three zones are arbitrary whereas the transition between the radial and the calcified zone is separated by an interface called tidemark which is a front of mineralization.

The calcified zone forms the connection between the cartilage and the subchondral bone as the collagen fibrils are linked to the bone. In the radial zone the collagen fibrils are thick with diameters of 100 to 140 nm and are aligned perpendicular to the bone cartilage interface. The fibrils in the transitional zone are arranged in a fuzzy structure. The amount of fibrils oriented parallel to the articular surface increases with decreasing distance to the articular surface. In the tangential zone which is located underneath the articular surface, the highest amount of parallel fibrils in regard to the articular surface is present [10]. The fibrils are thin (30–60 nm in diameter) and densely packed. Furthermore, the tangential zone is surrounded by the lamina splenden [34] which is a layer of fine fibrils with no cellular component. This keeps macromolecules larger than 6 nm from entering or escaping the cartilage matrix.

The height of the different zones varies from type to type of cartilage, within a cartilage plate and between different anatomical regions. Raya *et al.* measured the relative thickness of the

patellar cartilage with scanning electron microscopy (SEM). The radial zone was measured as (65±12)%, the transitional zone as (30±16)% and the tangential zone as (5±9)% [33]

The PG content in the tangential zone is at its lowest level where water is at its highest level. In the radial zone with the least amount of water [10, 35], the highest amount of PG is present. The concentration depends on the mechanical stress on the cartilage [36] and it decreases with age [22, 37-40].

The amount of chondrocytes is highest close to the articular surface in the tangential zone. They present an elliptical morphology with their principal axis being oriented parallel to the surface. In the transitional zone chondrocytes are mainly spherical and appear isolated, while in the radial zone they are enlarged, although sparse and usually forming columns. The concentration also differs with different anatomical locations [10, 29, 41].

2.2 Physiology

Cartilage possesses unique mechanical characteristics, which result from the balance between swelling pressure caused by the highly compressed and negatively charged PGs and the restraining forces applied by the collagen network.

The PGs in the articular matrix cause an osmotic pressure. However, due to the very densely packed PGs the osmotic pressure is non-ideal. Moreover, further osmotic pressure is generated by the high difference in Na^+ concentration between the extracellular matrix and the synovial fluid that is induced by the PGs [42, 43]. As described earlier, the PG distributes unevenly from the articular surface to the bone-cartilage interface in healthy cartilage. As a consequence there is a smooth gradient in osmotic pressure present (with the lowest value at the articular surface) which protects the collagen network from long term fatigue [42].

In equilibrium the osmotic pressure is balanced by the elastic force that is generated by the collagen network. In case of an external compression force being applied to the cartilage, the water is squeezed out of the superficial layers, dragging the cations with it. This causes the fixed negative charge of the GAGs to encounter a strong repulsive electrostatic force which compensates for the compressive stress [43, 44]. As soon as the external force is removed, the cartilage recovers rapidly. Hence, the deeper zones are responsible for the resistance to compressive forces whereas the architecture of the tangential zone with its parallel oriented collagen fibrils is in charge of resisting the shear forces of joint movement [10].

2.3 Osteoarthritis

A large part of the population older than 65 years is affected by OA. It is the most common joint disease and a big social and financial burden for most industrialized countries due to the high prevalence. As a consequence of OA the joint degenerates with the loss of cartilage. It is also accompanied by inflammation of the synovial capsule, fibrosis and subchondral bone alterations. Therefore, OA results in pain, joint stiffness and eventually functional impairment and disability of the joint.

2.3.1 Pathogenesis

Although the final mechanisms of cartilage degradation are still unknown, the basic pathogenetic process in OA is viewed as an imbalance between the synthetic and the degradative activity of chondrocytes. There are three overlapping stages in the process of cartilage:

Macromolecular degradation of cartilage matrix: It comes to a decrease of PG concentration at the articular surface and later also at the bone-cartilage interface [24]. Due to the PG loss, the osmotic pressure is redistributed along with additional mechanical stress in other regions of the collagen network [42].

Response of chondrocytes to the process of degradation: The change in the extracellular matrix also entails a change in osmolarity in the charge density and in the strain. The chondrocytes receive those changes as signals and react with increased metabolic activity. Hence, the synthesis of macromolecules is stimulated.

Failure of the chondrocytes in restoration of the cartilage, with premature apoptosis of the chondrocytes: The impact of the cytokines and the inflammatory mediators on the process of cartilage degeneration has been shown during the last few years [27, 45]. Cytokines hinder the collage synthesis and initiate the production of nitric oxide (NO) and metalloproteinases. The latter is responsible for the degradation of PG [27, 46]. NO serves as a fast messenger between cells and appears to be of importance in the inhibition of PG synthesis, metalloproteinase activation and the premature apoptosis of the chondrocytes [47, 48].

Due to the chondrocytes failing, there are changes in the joint structure and the loss of cartilage. The subchondral bone is exposed which results in the increase of the bone density. Bony growths called osteophytes develop that cause pain and also motion restrictions.

Furthermore, inflammatory reactions in the synovial fluid occur [49]. Eventually the patient experiences stiffness and weakness caused by the contraction of ligaments, capsules and muscles.

As there are no nerves in the articular cartilage, the pain is caused by the damage done by the cartilage loss to the joint structures, such as the subchondral bone or ligaments [48]. Thus it is not possible to determine the severity of the cartilage damage by looking at the severity of the symptoms.

2.3.2 Risk factors

There are several risk factors for OA. They can be divided into two groups the systemic risk factors and the local mechanical risk factors. Systemic risk factors concern any joint possibly affected by OA while local mechanical risk factors only concern one individual joint.

Although the relation between aging and OA is not certain, age seems to be the most relevant systemic risk factor for OA. The occurrences increase strongly with age [50]. Within the population of over 70 year olds, almost 60% suffer from OA [51]. However, OA is not just a consequence of aging of the cartilage [24, 50]. The prevalence in women is higher than the prevalence in men, especially after an age of 50 years. Hence, gender is an important factor as well [52]. There are other systemic risk factors, such as bone density and osteoporosis, genetic factors, and nutrition [51].

Among others, obesity, repetitive joint loading, joint instability, intra-articular deposition and muscle strength and weakness are some local mechanical risk factors [51].

2.3.3 Diagnosis

The standard method of diagnosing OA is the criteria developed by the American College of Rheumatology (ACR) which combines clinical symptoms, such as pain or joint stiffness and X-ray findings. The radiographic changes visible in OA are the formation of osteophytes, the narrowing of joint space and alterations in the subchondral bone [53, 54].

A grading scale to evaluate the severity of OA in the X-ray findings, called Kellgren and Lawrence classification, has been developed. The scale consists of 5 points with 0 representing no findings of OA. For grade I the X-ray shows doubtful narrowing of the joint space and possible osteophytes. X-ray findings of OA grade II present definite osteophytes and possible narrowing of the joint space. The severity is considered to be minimal. Patients

of grade III demonstrate multiple moderateley sized osteophytes, definite narrowing of the joint space and some sclerotic areas and possible deformations of bone ends. The OA is regarded to be moderate. A severe case of OA is represented by grade IV. Large osteophytes are visible in the X-ray images. Moreover, the joint space is considerably reduced and severe sclerosis and definite deformations of the subchondral bone are present [54, 55].

However, X-ray imaging is not sensitive to cartilage, which means cartilage is not visible on the X-rays. Hence, X-ray imaging does not correspond well with the clinical symptoms [51]. Furthermore, the findings may change with a different X-ray projection [56].

As post mortem studies assessed, the progress of osteoarthritis starts years before any radiographic changes are visible [57]. MRI may offer the diagnosis of early degeneration in the cartilage matrix and thus seems to be a very promising imaging method for OA.

2.3.4 Prevalence

The knee, hip and hand are the joints most frequently affected by OA. However, the spine and feet are also frequently involved whereas the wrist, ankles and shoulders can also be affected, but are commonly spared. Furthermore, it is not uncommon for more than one joint to be involved.

Studies about the prevalence in OA suggest that in a population of over 70 year olds more than 60% of male knees and more than 70% of female knees showed signs of OA, such as cartilage loss, subchondral bone alterations and osteophytes [51].

Due to OA developing several years before radiographic changes are visible, the prevalence determined through X-ray studies is lower than the prevalence determined through post-mortem studies.

2.3.5 Therapy

Unfortunately there is no known cure for OA. The treatment options are also very limited and ineffective. Treatment is divided into non-pharmacological and pharmacological therapy [54].

Non-pharmacological therapy: Non-pharmacological treatments are recommended as the first treatment option by most of the international guidelines [58-61]. They need to be individualized for each patient. An important part of the therapy is patient education where the patient and the patient's family and friends are taught how to manage the disease.

Furthermore, physical therapy plays an important role in the non-pharmacological treatment of OA. The therapist can show the patient how to avoid specific positions and movements that put too much force on the cartilage. An exercise program is commonly instructed to the patient to strengthen the musculature and to lose weight in case of overweight or obesity.

Pharmacological Therapy: This OA treatment focuses on the pain relief. The pharmacological therapy is applied in addition to the non-pharmacological treatments. When the pain is still low to moderate, paracetamol or acetaminophen and topical non-steroidal anti-inflammatory drugs (NSAID) are recommended. If the pain persists, opioid analgesics can be administered. With further progression of OA and the pain becoming moderate to severe, an aspiration and intra-articular injection of corticosteroid is recommended [54, 61].

The effectiveness of these treatments is highly dependent on how early in the progression of the disease the treatments are started. In many cases OA eventually limits the patient in their daily life and lowers their quality of life with pain, stiffness and reduced function of the joint. The recommended procedure in these cases is arthroplasty where the joint surface is partially or totally replaced by prosthesis to recover joint motion.

3. MRI of articular cartilage

MRI is a non-invasive and radiation-free imaging method. Its soft tissue contrast cannot be matched by any other method and it is possible to show excellent anatomical detail of the joint. MRI provides excellent contrast in cartilage imaging. Hence, it has many advantages for imaging the joint.

In the early stages of OA, the components of the extracellular matrix are first affected. The amount of PGs decreases and the integrity of the collagen network changes. The focus of many researchers has been on developing MRI methods to non-invasively detect those changes in the extracellular matrix of the cartilage. In the following sections, the most relevant methods for the detection of PG concentration and collagen are described.

3.1 MRI of proteoglycans

PGs are highly negatively charged due to their GAG side chains. The charge in the matrix due to the GAG is called fixed negative charge. The free-mobile ion concentration in the cartilage is determined by that fixed charge. It is not possible to directly measure the PG content. However, it is possible to detect the free-mobile ion concentration of ions, such as Na^+ or $Gd(DTPA)^{2-}$. Furthermore, the macromolecules in the extracellular matrix cause restricted motion of the water molecules. If the concentration of PG changes and the restriction of the water molecule mobility also changes, this can be detected with diffusion measurements. $T_{1\rho}$ imaging is also sensitive to the PG content [62-64].

3.1.1 Sodium MRI

Due to the high negative charge of PG in the cartilage, a high concentration of Na^+ cations is also present in the cartilage. The sodium distributes in relation to the distribution of GAG and is thus highly sensitive to GAG. The sodium distribution can be detected by Na^+-MRI. Hence, information about the GAG and therefore the PG concentration can be derived [63]. In Fig. 4 an overlay of proton images with the sodium maps is illustrated. There clearly is a lower sodium signal in the OA cartilage in comparison to the healthy cartilage. Due to the GAG concentration determining the sodium signal, there is a lower GAG concentration in the OA cartilage present which coincides with the cartilage degeneration.

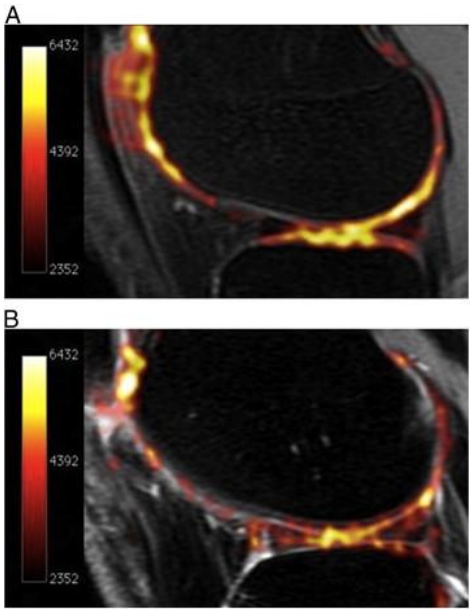

Figure 4: Sodium maps overlaid onto proton images of articular cartilage in a healthy subject (A) and an OA subject (B) (adapted from [1])

However, the gyromagnetic ratio of sodium is different with γ_{Na}= 11.3 MHz/T, *i.e*. 26% of the proton gyromagnetic ratio. Therefore, the images cannot be acquired with the same hardware as proton MRI. Moreover, in comparison to proton based MRI imaging, the resolution achievable with sodium imaging is significantly less. Due to the need for different hardware, Na^+-MRI is not available on most clinical scanners. Nevertheless, Na^+-MRI for the early detection of OA is of high importance. Sodium being a native cation in the human body and always being in equilibrium are clear advantages [63].

3.1.2 Delayed Gadolinium Enhanced MRI of Cartilage (dGEMRIC)

Determining the fixed negative charge of the extracellular matrix using the contrast agent $Gd(DTPA)^{2-}$ works similarly to determining it through the Na^+ concentration. Compared to the positive charged Na^+, the contrast agent $Gd(DTPA)^{2-}$ has a negative charge. This results in $Gd(DTPA)^{2-}$ distributing inversely proportionally to the GAG distribution in the cartilage due to the contrast agent being repelled by the GAG. The T_1 relaxation time is determined by the concentration of the contrast agent due to $Gd(DTPA)^{2-}$ reducing T_1. Hence, the distribution of $Gd(DTPA)^{2-}$ can be detected by measuring the T_1 relaxation time in cartilage, thus information about the GAG and PG content can be derived. Assessing GAG in the cartilage with $Gd(DTPA)^{2-}$ was first introduced by Bashir *et al.* in 1996 and is called Delayed Gadolinium-Enhanced MRI of Cartilage (dGEMRIC) [63, 65]. In Fig. 5 a comparison of the cartilage of a

healthy knee and an OA knee is illustrated. The scale for the T_1 relaxation time and thus the dGEMRIC index is in milliseconds. The OA clearly presents lower values, especially in the areas pointed out by the white arrows. That means the $Gd(DTPA)^{2-}$ concentration is higher in those areas and thereby the GAG content lower, which coincides with the OA characteristics [2].

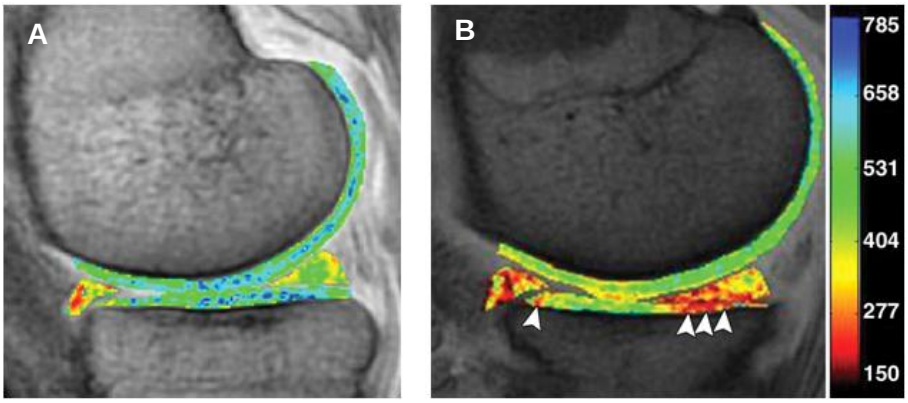

Figure 5: Comparison of dGEMRIC index in a knee of A) a healthy subject and B) an OA subject (white arrows pointing out lower values in OA subject, adppted from [2])

The contrast agent has to be injected intravenously. Before the MRI examination can be conducted, it has to access the cartilage. The concentration is assumed to be balanced in the joint after 90 minutes [66].

dGEMRIC provides reasonably high resolution and can be implemented on clinical scanners [63]. Hence, it is of high importance for the early detection of OA with MRI. Nevertheless, having to inject the contrast agent and the long wait of 90 minutes for the $Gd(DTPA)^{2-}$ to be balanced in the joint are strong disadvantages.

3.1.3 $T_{1\rho}$ imaging

The $T_{1\rho}$ parameter represents the spin-lattice relaxation time in the rotation frame. $T_{1\rho}$ imaging was first introduced by Redfield in 1955 in solids [67] and later extended to liquids by Bull [68]. The $T_{1\rho}$ relaxation time is determined by the interaction of the macromolecules in the extracellular matrix and the motion-restricted water molecules. As mentioned before, the restriction in motion of the water molecules is predominantly caused by the PG and collagen content in the cartilage [64]. Hence, if the PG content changes, the $T_{1\rho}$ relaxation time will also change, thus $T_{1\rho}$ is also sensitive to early degeneration of cartilage. Significantly higher $T_{1\rho}$ values were measured in OA subjects compared to healthy controls in several studies [69-71]. In Fig. 6 the increase in $T_{1\rho}$ is illustrated. The mean $T_{1\rho}$ in the medial femoral condyle

was 32.9±9.0 ms for the healthy control in a), 41.1±11.0 ms for the OA patient with Kellgren and Lawrence grade I in b) and 49.1±14.2 ms for the OA patient with Kellgren and Lawrence grade III in c). The values in the medial tibia were 35.8±11.4 ms for the healthy control, 39.3±12.2 ms for the subject with moderate OA and 43.6±12.0 ms for the subject with severe OA [64].

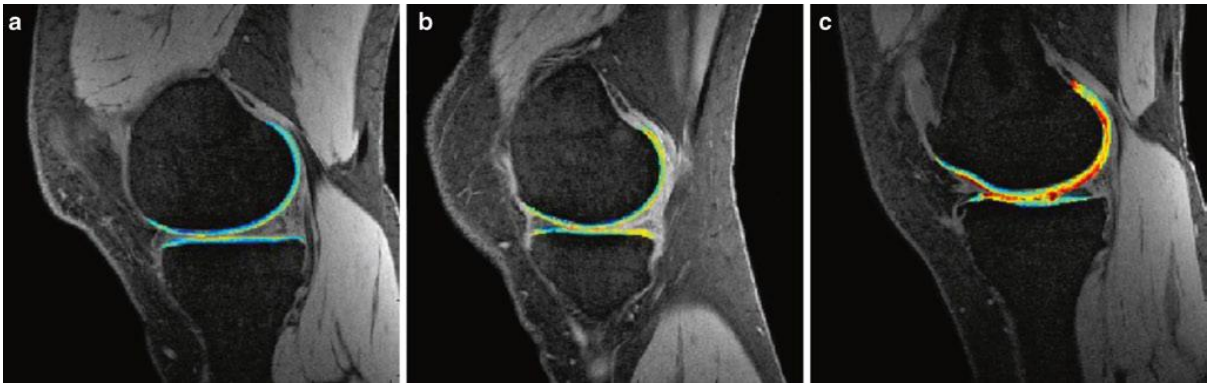

Figure 6: $T_{1\rho}$ maps in knee cartilage of a) healthy control, b) a patient with mild OA and c) a patient with severe OA (adapted from [64])

A contrast agent or additional hardware is not needed for $T_{1\rho}$ imaging. However, the relaxation mechanism of $T_{1\rho}$ seems to be unspecific. Furthermore, the acquisition times were long and the limitations of the specific absorption rate (SAR) were a challenge and make the use in a clinical environment difficult. Nevertheless, recent developments in MRI, such as parallel imaging, have managed to overcome those limitations and have led to the use of $T_{1\rho}$ imaging in clinical scanning.

3.2 MRI of the collagen network

3.2.1 T_2 imaging of cartilage

The T_2 relaxation time in cartilage is determined by the interaction between water molecules itself and between water molecules and macromolecules in the extracellular matrix. Where $T_{1\rho}$ is sensitive to the proteoglycans, T_2 is sensitive to the collagen in the matrix. The loss of collagen leads to the hydration of the cartilage which in turn leads to the water molecules moving more freely [72]. This results in an increase of T_2 in the areas with collagen loss. Several studies were able to determine a significant increase in T_2 in OA cartilage compared to healthy cartilage [73-76]. In Fig. 7 T_2 maps of a healthy subject in a) and an OA patient in b) are illustrated. The color coded maps show the increased T_2 values in the OA cartilage in comparison to the healthy cartilage.

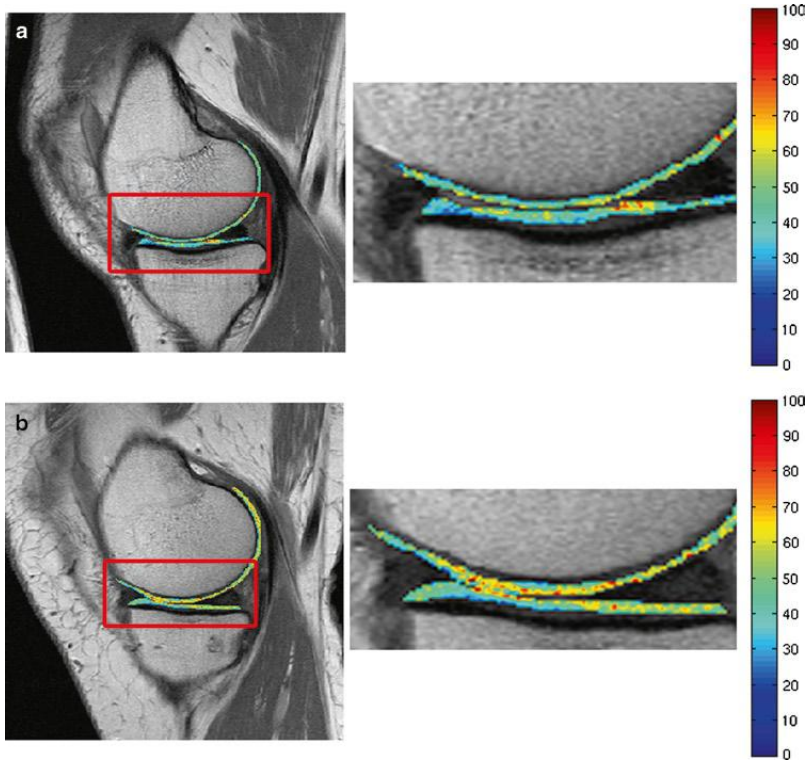

Figure 7: T_2 maps in ms of a) a healthy subject and b) an OA subject (adapted from [72])

Collagen is affected in the early stages of OA. Hence, T_2 measurements seem to be an effective method to gain insights into the cartilage of a patient and to diagnose OA early. However, T_2 is not completely specific to collagen, but also to water concentration and partially to PG and the T_2 values are highly dependent on the T_2 calculation technique. Furthermore, while T_2 can detect cartilage degeneration in early stages it cannot provide any information about the severity of the OA which means that no difference between the OA grades can be seen [72, 73].

3.3 MRI sensitive to proteoglycans and collagen

The methods described in the sections above are only sensitive to either proteoglycans or collagen. As both these components are affected in the early stages of OA, it would be of great advantage to have an imaging technique that is sensitive to both PG and collagen. Diffusion Tensor Imaging is such a method. Changes in the extracellular matrix, specifically in PG content or collagen network, result in a change of motion restriction of the water molecules. DTI is able to provide information about the PG content with the mean diffusivity (MD) and the collagen architecture with the fractional anisotropy (FA) which will be discussed later [3, 77].

3.3.1 Quantitative morphology

As the cartilage degrades with OA it changes its morphology. Hence, observing and assessing the changes in morphology of cartilage is used to monitor OA. Among others this includes measuring the cartilage thickness and volume, evaluating the area of the articular surface, the bone-cartilage interface, the denuded subchondral area and the lesion size. High resolution images with good contrast between cartilage and adjacent tissue are necessary to assess the morphology of the cartilage. Due to the thickness and volume of cartilage not being determined by the matrix component, measuring thickness and volume does not help in the early detection of OA. Nevertheless, it has given valuable information about the risk factors influencing OA [78-81].

3.3.2 Diffusion

Diffusion is a physical process where particles move due to their thermal energy. Macroscopically, the law that describes this motion is called Fick's first law [82].

$$J = -D\nabla C \tag{3.1}$$

where J is the net particle flux, C the particle concentration, D the diffusion coefficient and ∇ the gradient operator. As seen in Eq. 3.1 the flux rate is proportional to the diffusion coefficient and the concentration gradient. According to Fick's law in the absence of concentration gradients there is no net particle flux J. Furthermore, the law describes the tendency of particles to move from a region with high concentration to a region with low concentration, hence the negative sign in the equation [83].

Microscopic motion due to thermal energy is referred to as Brownian motion. The molecules move in opposite directions with equal probability and therefore the average distance that the molecules travel equals zero. Albert Einstein introduced the quadratic average displacement to evaluate the movement of particles [83]. Einstein's equation (Eq. 3.2) provides a microscopic interpretation to Fick's law.

$$\langle r^2 \rangle = 2D\Delta \tag{3.2}$$

where r is the distance traveled by the particles, Δ the diffusion time during which the particles are moving and D the diffusion coefficient.

In free water, the particles can move in each direction with the same probability and their motion is not restricted in any direction. This is referred to as isotropic diffusion. However, in

biological tissue, the water molecules collide with contents of the extracellular matrix, such as cell membranes, PG or collagen. This directionally restricts the movement of the water molecules and is referred to as anisotropic diffusion. PG restricts the water molecules equally in each direction and thus determines the mean diffusivity (MD) whereas collagen modifies the fractional anisotropy (FA) by favoring the motion along its fibers. These parameters can be measured with Diffusion Tensor Imaging (DTI). Hence, DTI provides important insights not only into changes in PG content by measuring the MD, but also into the collagen architecture by measuring the FA. The sensitivity to both PG and collagen makes DTI a valuable method to detect changes in the extracellular matrix.

3.3.3 Diffusion-Weighted Imaging (DWI) and Diffusion Tensor Imaging (DTI)

The first DWI studies were on neurological disorders [84] and the first breakthrough in showing the importance of DWI for diagnostic purposes was in acute stroke. Strokes can be caught within minutes of their onset [85]. DWI also appears to be very promising in the differentiation of benign and malignant acute vertebral fractures [86-89].

Diffusion-Weighted Imaging

In 1965 Stejskal and Tanner introduced the Stejskal and Tanner sequence to quantitatively determine the diffusivity in the tissue, the so-called apparent diffusion coefficient (ADC). It is also known as pulsed-gradient spin echo sequence (Fig. 8) and is commonly used for diffusion sensitized pulse sequences [90]. The idea is to apply two identical gradients, the diffusion gradients, at either side of the refocusing radio frequency (RF-) pulse. “Identical” means they are of the same polarity and have equal magnitude (G) and duration (δ).

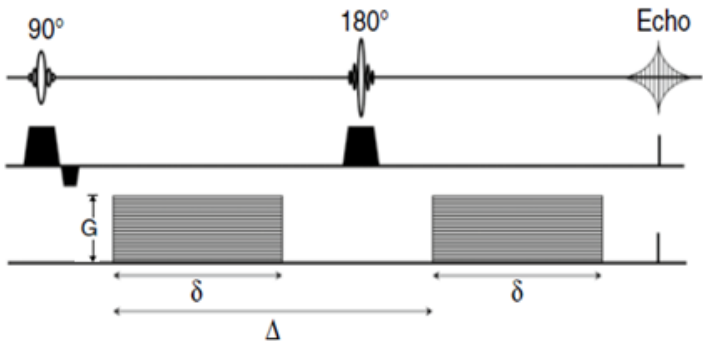

Figure 8: A pulsed-gradient spin-echo sequence after Stejskal and Tanner (adapted from [83])

The diffusion gradients produce a position dependent dephasing and rephrasing of the spins. The spins that are not in motion in the direction of the diffusion gradient are refocused completely whereas the spins in motion, the diffusing spins, obtain different phases during the first and second gradient. Therefore, the diffusion of the spins leads to a net dephasing of the MRI signal at the echo time, causing signal attenuation dependent on the mobility of the spins. While spins with small diffusivity only lead to a small attenuation in signal intensity, spins with large diffusivity will lead to a higher signal loss. Hence, the signal intensity shows an exponential dependence on the ADC, as illustrated in Eq. 3.3.

$$S = S_0 e^{-b \cdot ADC} \tag{3.3}$$

where S is the observed signal intensity obtained with a certain diffusion-weighting, S_0 is the signal intensity without the application of a diffusion gradient and *b* is the *b*-value, a measure of the diffusion-weighting due to the sequence parameters:

$$b = (\gamma G \delta)^2 (\Delta - \frac{\delta}{3}) \tag{3.4}$$

The *b*-value is determined by the gyromagnetic ratio γ and the diffusion gradient parameters, the amplitude G, the duration δ and the diffusion time Δ which describes the separation between the onset of the two diffusion gradients as illustrated in Fig. 8.

To calculate the ADC, several images (at least two) of the same slice with different *b*-values have to be acquired. By using exponential fit or linear regression analysis, the ADC can then be calculated, either by looking at the mean intensity of a region or in a pixel-by-pixel manner. The pixel-by-pixel analysis will result in an image where each pixel represents an ADC value, also known as the ADC map.

The diffusion gradients are applied in certain directions. Only motion in this direction leads to signal attenuation in the diffusion-weighted image. If the diffusion is isotropic, thus constant in all directions, one measurement in one direction describes the diffusion sufficiently. However, biological tissue is not isotropic, therefore more than one measurement is needed to characterize diffusion in the tissue.

Diffusion Tensor Imaging

By applying the diffusion gradients in several directions, the ADC can be calculated in different directions. For low *b*-values and avascular tissues the spatially varying ADC is accurately described by a 3×3 symmetrical matrix of diffusion coefficients: the diffusion tensor.

$$D = \begin{bmatrix} D_{11} & D_{12} & D_{13} \\ D_{12} & D_{22} & D_{23} \\ D_{13} & D_{23} & D_{33} \end{bmatrix} \tag{3.5}$$

As seen in Eq. 3.5 the diffusion tensor has only six different components. For isotropic media, the tensor is diagonal with the same values for each component due to the diffusion being the same in all directions, so that only one diffusion constant characterizes the isotropic media.
In case of anisotropic diffusion, the tensor can be diagonalized which will provide three eigenvectors ($\vec{v}_1, \vec{v}_2, \vec{v}_3$) with associated eigenvalues ($\lambda_1, \lambda_2, \lambda_3$). The eigenvalues are always non-negative. Graphically, the tensor can be interpreted as an ellipsoid (Fig. 9), with the eigenvectors representing the one major and two minor axes and the eigenvalues representing the lengths of the axes [83]. If the diffusion is isotropic, the three eigenvalues have the same value and the ellipsoid becomes a sphere.

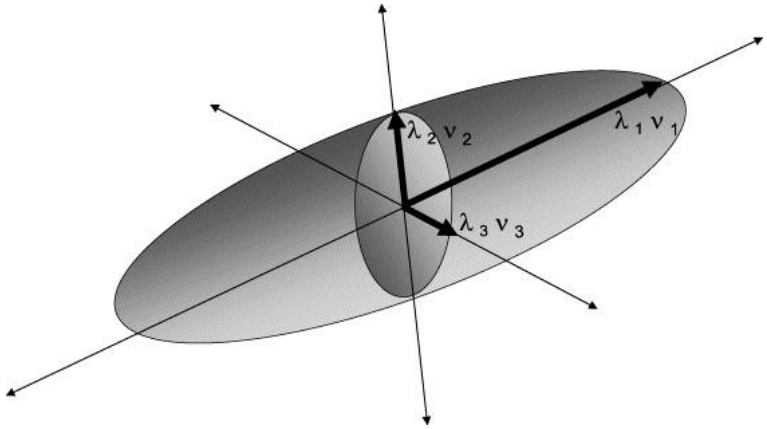

Figure 9: Graphical interpretation of diffusion tensor, with the eigenvectors ($\vec{v}_1, \vec{v}_2, \vec{v}_3$) representing the axes and the eigenvalues ($\lambda_1, \lambda_2, \lambda_3$) representing the length of the axes (adapted from [91])

To calculate all the components of the diffusion tensor, at least six measurements in different (non-parallel) directions have to be performed [92].

The diffusion tensor provides several DTI parameters. The mean diffusivity (MD) represents the diffusivity averaged over all spatial orientations. It can be calculated with the trace of the sensor, which is the sum of the diagonals, thus D_{11}, D_{22}, and D_{33}, as illustrated in Eq. 3.6.

$$MD = \frac{1}{3} \cdot Trace(D) = \frac{\lambda_1 + \lambda_2 + \lambda_3}{3} \tag{3.6}$$

The most common parameter to evaluate the anisotropy of the diffusivity is the fractional anisotropy (FA). It assesses the fraction of the tensor that is ascribed to anisotropy and is calculated as described in Eq. 3.7.

$$FA = \sqrt{\frac{3}{2} \cdot \frac{(\lambda_1 - MD)^2 + (\lambda_2 - MD)^2 + (\lambda_3 - MD)^2}{{\lambda_1}^2 + {\lambda_2}^2 + {\lambda_3}^2}} \quad (3.7)$$

FA is normalized to values between 0 and 1, where 0 represents completely isotropic diffusion.

The first diffusivity values in healthy and pathological cartilage were invasively obtained by Maroudas *et al.* They measured diffusivity in healthy cartilage, $1.30 \times 10^{-3} mm^2/s$, and OA cartilage, $1.45 \times 10^{-3} mm^2/s$, at 37°C [93, 94]. The first ADC maps showed an increase in the diffusivity from the bone-cartilage interface to the articular surface in both human [95] and canine cartilage [96]

Several studies focused on the artificial degradation of GAG and collagen. Burstein *et al*. treated healthy calf cartilage with trypsin and found an increase in ADC of water after GAG depletion [97]. Xia *et al.* also received a significant increase in ADC after artificial GAG and collagen depletion in human cartilage [96]. However, artificial degradation process is different from the natural degradation. Mlynárik *et al.* correlated histological cartilage slices with signs of OA with ADC maps and found a significant increase in comparison with healthy areas [98].

Ex vivo DTI studies established diffusion anisotropy in human and bovine cartilage. Filidoro *et al.* demonstrated that the first projection vector, which represents the major axis of the tensor ellipsoid, had a clear zonal pattern with the orientation tangentially in the upper and radially in the lower portions of the human cartilage [3, 77]. This was confirmed in bovine cartilage [4, 99]. The findings correlated with the known zonal pattern of cartilage. To prove the assumption that the anisotropy is determined by the collagen structure, the data derived with DTI was correlated with scanning electron microscopy on human samples [33, 100] and with polarized-light microscopy in bovine patellar cartilage [4, 99]. Strong correlations were found. Raya *et al.* investigated samples with early cartilage damage. The damage in the cartilage samples was assessed with the histology OARSI score. DTI of these samples provided excellent results in the detection of cartilage damage and good results in grading the cartilage in relation to the histology findings [101].

Recent *in vivo* DTI studies demonstrated its importance for the early detection of OA [3, 4, 77]. Raya *et al.* were able to detect a significant increase in MD and a significant decrease in FA in the OA subjects in comparison to the healthy controls [9, 102].

In summary, DTI can provide information about both the PG content and the collagen structure through MD and FA. DTI is also sensitive to cartilage degradation and has shown promise as a biomarker for early cartilage degeneration *in vivo*. However, the clinical application of DTI is still limited, as first results were acquired in non-clinical magnets [9] or with lack of good image quality and resolution [6-8]. Therefore it is of utmost importance to develop new methods for acquisition of high resolution DTI datasets on clinical scanners. This is the motivation of the present work.

4. Implementation of RAISED sequence

In vivo DTI of articular cartilage is still very challenging. For measurements to be performed in a clinical environment, the scan time should not exceed 20 minutes. However, for a DTI dataset at least six diffusion-weighted and one non-weighted image have to be acquired. The use of rapid-acquisition techniques, such as DW-EPI or DW-HASTE, only provides low resolution images. However, high resolution images are needed to assess the integrity of the thin cartilage layer. Also, the complex anatomy of the knee with many tissue interfaces causes susceptibility jumps which lead to distortions on the EPI images. Additionally, the low T_2 values in cartilage make the use of rapid-acquisition techniques difficult. Therefore, a fast and robust sequence which is not sensitive to motion and offers high quality images would be desirable. In this work I propose to use a radial spin-echo sequence to acquire the DTI data.

4.1 Radial sampling

While in Cartesian acquisition the *k*-space rows are sampled in parallel rows, the *k*-space data in radial sampling is acquired radial along so-called spokes (Fig. 10). These spokes all cross the center of *k*-space.

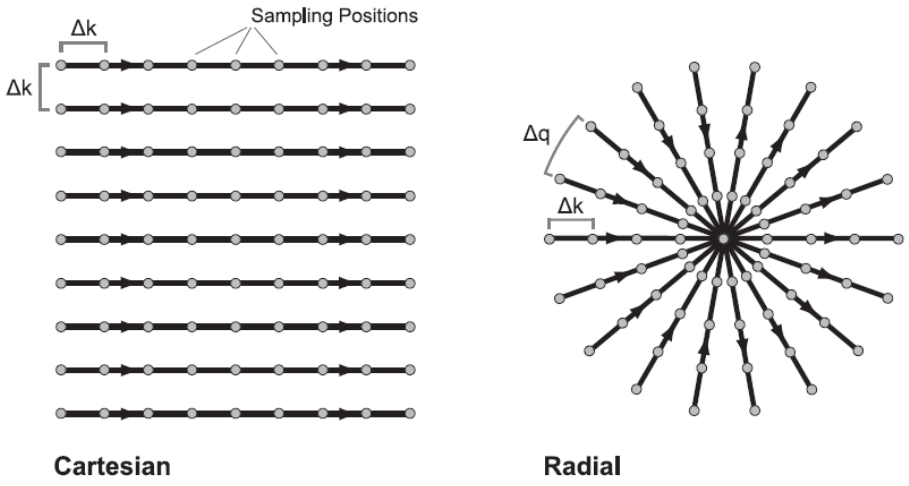

Figure 10: Cartesian and radial sampling (adapted from [103])

The spokes that differ from the angle of zero degrees can be generated with a combination of the gradients in x- and y-direction [104]. Hence, they are a rotation of the zero degree spoke around the *k*-space center. As seen in Fig. 11 the gradients G_x and G_y are changing with every acquisition, indicated by the lines inside the gradients.

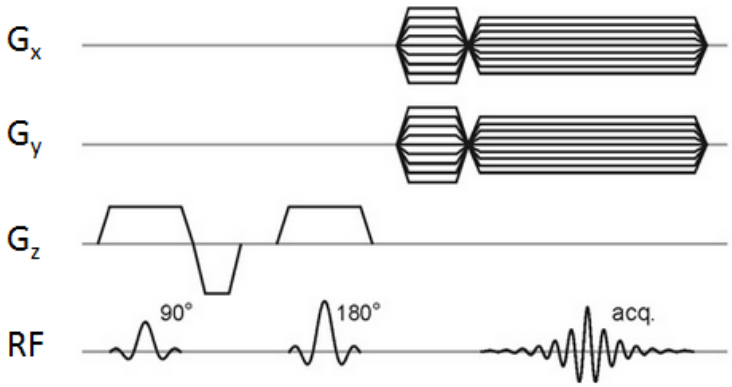

Figure 11: Radial spin echo timing diagram (adapted from [105])

The gradients in the two directions can be calculated in the following way:

$$G_x = G_0 \cdot \cos(\theta) \qquad G_y = G_0 \cdot \sin(\theta) \tag{4.1}$$

with G_0 being the gradient for the zero degree spoke, G_x and G_y the projections in the x- and y- coordinates, and θ being the angle of the spoke in respect to the central *k*-space row [104].

In Cartesian sampling the number of sample points along one line is determined by the base resolution n and the distance between two samples. The sampling has to fulfill the Nyquist criterion.

$$\Delta k = \frac{1}{FOV} \tag{4.2}$$

To ensure that the distance between samples on neighboring spokes Δq is less or equal to Δk, the number of spokes, n_s, has to be:

$$n_s = \frac{\pi}{2} \cdot n \tag{4.3}$$

Since all the spokes cross the center of the *k*-space, the sample density in the center of *k*-space is much higher compared to the density of sample points further away from the *k*-space center [106], which has to be considered in the reconstruction of radial images.

4.2 Image reconstruction

Gridding

The most common method to reconstruct an MR image is by Fourier transforming the data acquired in *k*-space. However, fast versions of the Fourier transforms can only be applied to data in Cartesian grids. As illustrated in Fig. 12, the radial sampling points, represented by the black circles, do no match the Cartesian grid points, represented by the plus signs. Thus the data acquired by radial sampling has to be mapped to the Cartesian grid. Gridding is the method used to interpolate the radial data onto a Cartesian grid.

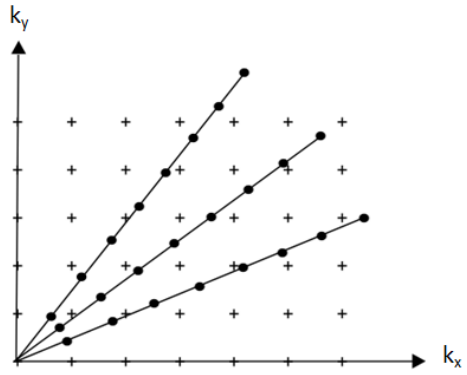

Figure 12: Radial sampling points on a Cartesian grid (+)

The first step in the gridding process is density compensation as the sample density in the center of *k*-space is higher than in the outer parts of *k*-space. This leads to more sample points contributing to an interpolated data point in the center of *k*-space than in areas further away. To compensate for this, a ramp filter $\xi(k_r)$ can be applied to the raw data $F(k_r, k_\theta)$ before interpolating it (Eq. 4.4). A ramp filter is a linear weighting function that weights each sample point. This process is also known as pre-compensation.

$$F_D(k_r, k_\theta) = \frac{F(k_r, k_\theta)}{\xi(k_r)} \tag{4.4}$$

The pre-compensated data $F_D(k_r, k_\theta)$ can then be mapped to a Cartesian grid. This is done by convolving the pre-compensated data with a gridding kernel in the frequency space.

$$F_S(k_x, k_y) = W(k_x, k_y) * F_D(k_r, k_\theta) \tag{4.5}$$

where $F_S(k_x, k_y)$ is the data mapped to a Cartesian grid and $W(k_x, k_y)$ is the gridding kernel. The gridding kernel that is used has a high impact on the results as it determines how points

are distributed over the Cartesian grid. Hence, it is responsible for how much each polar sample contributes to the neighboring Cartesian grid points. The Fourier transform of the gridding kernel is called window function and is responsible for the field of view (FOV) of the resulting image. In order to avoid any image distortion, the window function needs to be as close to a rectangular function as possible. The multiplication of a compact signal with a rectangular function does not lead to blurring, thus the ideal gridding kernel would be a sinc function (Fig. 13).

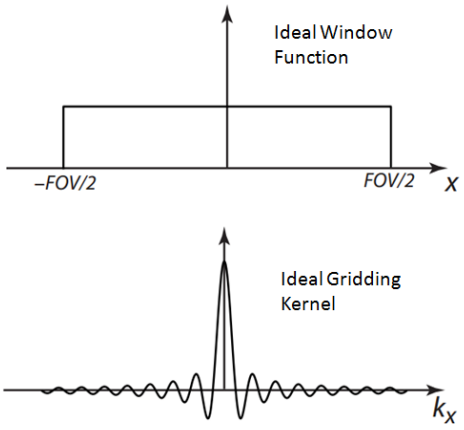

Figure 13: Ideal gridding kernel and its window function (adapted from [107])

However, with regard to computational speed it is not efficient to implement a sinc function. A good approximation of a sinc interpolation kernel is the Kaiser-Bessel function kernel [108, 109] which is given by

$$W_{KB}(k_x, k_y) = \begin{cases} \frac{1}{L} I_0\left(\beta\sqrt{1-\left(\frac{2|\vec{k}|}{L}\right)^2}\right) & |\vec{k}| \leq \frac{L}{2} \\ 0 & |\vec{k}| > \frac{L}{2} \end{cases} \tag{4.6}$$

where L is the kernel width, I_0 the zero-order modified Bessel function of the first kind, and β a shape parameter which can be selected accordingly. Its window function contains small side lobes compared to other window functions that can be used. Hence, aliasing effects can be minimized. The Kaiser-Bessel function and its window function with only the main lobe are illustrated in Fig. 14.

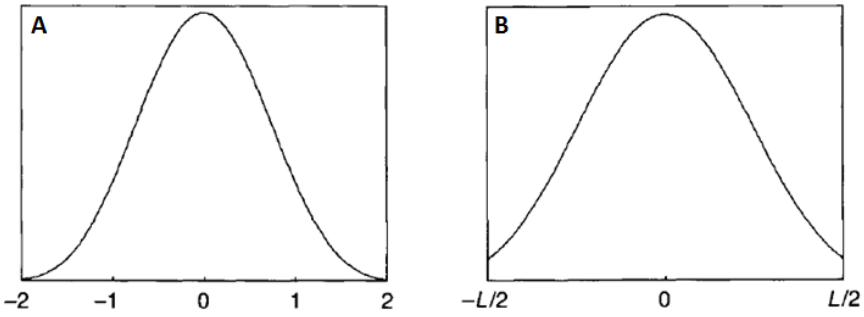

Figure 14: A) Kaiser-Bessel function with width of 4 B**)** Corresponding window function (only the main lobe, adapted from [106])

The data has to be corrected for small inhomogeneities in the sampling density. These inhomogeneities remain after pre-compensation. During the convolution along with the gridding of the *k*-space a density matrix is computed. This matrix contains the contribution of all the polar data points to all Cartesian data points. To rid the data of the remaining inhomogeneities this density matrix is used. This process is known as post-compensation and is performed as follows:

$$F_w(k_x, k_y) = \frac{F_S(k_x,k_y)}{\rho(k_x,k_y)} \tag{4.7}$$

with $F_w(k_x, k_y)$ being the post-compensated data and $\rho(k_x, k_y)$ the density matrix.

Now the interpolation process is complete and the data can be inverse Fourier transformed using the efficient fast Fourier techniques (FFT):

$$f_w(x, y) = \mathcal{F}^{-1}\{F_w(k_x, k_y)\} \tag{4.8}$$

Convolution in frequency space corresponds to multiplication in image space. As the convolution with the gridding kernel in Eq. 4.5 was performed in frequency space it corresponds to the multiplication of the final image by the inverse Fourier Transform of the gridding kernel. Therefore, in order to obtain the final image $f(x, y)$, the inverse Fourier transform (FFT) of the post-compensated data $f_w(x, y)$ has to be divided by the window function of the gridding kernel $w(x, y)$, which is the inverse Fourier transform of Eq. 4.6:

$$f(x, y) = \frac{f_w(x,y)}{w(x,y)} \tag{4.9}$$

It is also common to use oversampling due to the interpolation kernel not being ideal. The final image then has to be cropped after the inverse FFT.

Iterative Reconstruction

To reduce scan time, undersampling is commonly used. In radial acquisition this can lead to streaking artifacts, but the data can be corrected by using iterative reconstruction [110]. The reconstruction method was developed for a data set with a much lower number of spokes than the required number by the Nyquist criterion. It is based on gridding, which was explained above. In this case the problem is that the system is highly underdetermined which means that not all *k*-space positions are covered by the sampling points along the spokes. As a consequence of indetermination there can be more than one solution for the acquired *k*-space data and it is impossible to evaluate which solution is the correct one, so that more advance techniques are required.

In the iterative reconstruction the image is estimated and the difference to the actual data computed. This difference is used as the goodness of fit to assess the quality of the image reconstruction, the smaller the difference, the better the fit. This step is done iteratively, until the difference is minimized. To select among all possible solutions, an additional factor called penalty is added to the reconstruction algorithm, which penalizes solutions with undesired properties such as streaks. However, it requires knowledge about the imaged object beforehand. To make it vastly practicable, the penalty criteria need to be of broad applicability to many situations [110].

When working with radial MRI data, the most applicable penalty to our data is an approach presented by Rudin *et al.* in 1992. It was initially used for noise removal and is based on restricting the total variation (TV) [111]. An image is assumed to consist of areas with constant or mildly varying intensity. However, the image estimates from undersampled radial images are affected by streaking artifacts, which lead to sharp edges. Hence, the TV in these estimates is high. Therefore, the best image estimation is given by the estimate with the lowest TV [110]. For reconstructing images with the iterative reconstruction method, the number of iterations and the strength of the TV regulation can be chosen.

4.3 MRI System and implementation on Siemens Scanner

The RAISED sequence was implemented on a 3 T scanner (MAGNETOM Skyra, Siemens AG) using the IDEA software (VD13 baseline 11 November 2012). The Skyra has a gradient strength of 45 mT/m and a maximum slew rate of 200 mT/m/s. To avoid eddy currents, a moderate slew rate of 100 mT/m with a maximum gradient strength of 35 mT/m was used. Furthermore, besides the diffusion time Δ and the diffusion gradient duration δ an additional parameter was introduced to separate the diffusion gradient from the refocusing pulse and the readout gradient to ensure no interference of the diffusion gradient with the slice selecting gradient during the refocusing pulse and the readout gradient. The diffusion weighting was chosen by setting the *b*-value, and then the G and diffusion gradient duration δ were calculated for the given diffusion time Δ.

By optimizing the MRI protocol the best settings for parameters such as TE, resolution, TR and the *b*-value were determined (see chapter 6.1). For obtaining DTI datasets, the diffusion gradients were applied in six isotropically distributed directions (six directions diffusion-gradient schemes found with downhill simplex minimization [112]).

4.4 Advantages and disadvantages of radial sequences

Multi-shot Cartesian sequences are very susceptible to motion artifacts. This can result in ghosting artifacts very close to the moving object and the diagnosis can be altered. Furthermore, acquiring less *k*-space samples and thus accelerating the sequence leads to aliasing artifacts or reduced resolution. This results in multi-shot Cartesian sequences having long acquisition times. Single-shot Cartesian sequences on the other hand acquire the data within seconds, although with low image quality and image distortions.

Radial sequences are very motion robust. In comparison to Cartesian sequences, the readout direction constantly changes and the *k*-space center is oversampled. Thus, differences due to motion between spokes lead to less pronounced artifacts [113]. Radial sampling results in a higher *k*-space density in the center of *k*-space (low spatial frequencies) due to all spokes crossing the origin. Since the *k*-space center holds the most information about the object, acquisitions with only a few spokes are possible. Undersampling a radial sequence introduces streaking artifacts to the image. However, these streaking artifacts are of low intensity and are located at the border of the image, further away from the region of interest, which makes them more tolerable in diagnostics [104]. Furthermore, the streaking artifacts can be compensated by using advanced reconstruction methods as explained above [110].

Hence, radial sequences are of high importance if acquiring images in a short time is necessary.

Acquiring images with an accelerated radial sequence will also lead to increased noise which will reduce the SNR. Thus, the imaging protocol has to be chosen carefully to receive sufficient SNR, especially in our case where sufficient SNR is important for the correct calculation of the diffusion parameters. However, the changing readout direction in radial sampling also has its drawback. Inconsistencies due to eddy currents are not the same in each acquisition as they are in Cartesian sampling, therefore they will appear in the images as blurring. Hence, it is of high importance to check for eddy currents and possibly compensate for them. Due to the clinical limitation of scan time and the need for good resolution images, radial sequences seem to be of high importance for imaging articular cartilage.

5. Calibration of RAISED sequence

In order for a sequence to be applicable in clinical scanning, it has to fulfill several requirements. The scan time should not be more than 20 minutes, yet at the same time the quality of the images and the results need to be feasible. Therefore, the sequence needs to be calibrated. This includes checking for eddy currents, comparing the result to images acquired with a Cartesian sequence and checking whether sequence acceleration still provides feasible images.

5.1 Eddy Currents

Theory

Eddy currents appear due to the rapid switching of the gradient pulses. The stronger the gradient pulses are, the more pronounced the eddy currents will be. In diffusion-weighted imaging, strong diffusion sensitizing gradients that are switched on and off are necessary. This generates a time varying magnetic field which can cause a current induction in the conductive structures of the MR scanner. The currents then generate an additional magnetic field which may persist even after the gradients are switched off. This results in an altered shape of gradient pulses, represented by the red line in Fig. 15 as compared to the presumed gradient shape in green, causing the expected *b*-value to differ from the nominal *b*-value [114]. The eddy current can also superimpose to other imaging gradients leading to image distortions such as contraction, dilatation, shifting or shearing of the image. The diffusion gradients may also overlap with the phase encoding gradient or the readout gradient which can cause additional geometric distortions and inconsistencies in the signal intensity [114]. This is illustrated by the red line overlapping the readout gradient in yellow in Fig. 15. The diffusion gradients are applied before and after the refocusing pulse. If the diffusion gradient persists due to eddy currents and is applied too closely to the refocusing pulse, it may also overlap with the slice selecting gradient (blue in Fig. 15) which would cause imperfect slice excitation and thus errors in slice profiles.

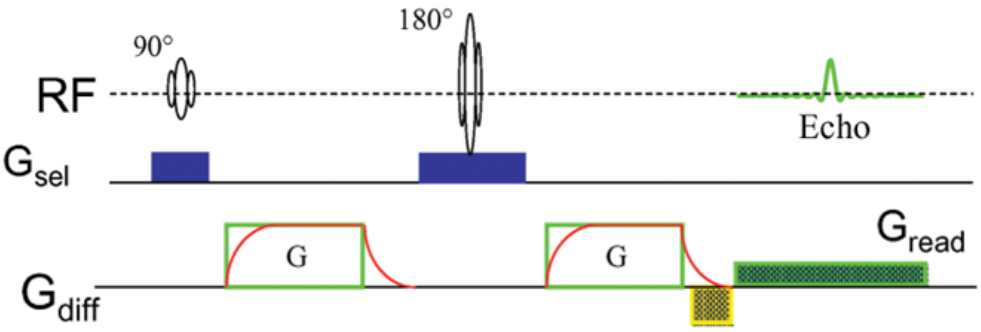

Figure 15: Eddy current effects, with the actual shape of the diffusion gradient altered by eddy currents in red as compared to the expected shape in green. The altered diffusion gradient can interfere with the readout gradient in yellow or the slice selecting gradient in blue [114]

In DTI diffusion gradients are applied in at least six different directions so that the image may be affected by eddy currents differently in each diffusion weighting. Furthermore, the readout gradient in radial sampling changes for every spoke so that even within one image eddy currents can cause blurring due to the different effect on each spoke. Since the diffusion parameters are calculated with at least two different applied gradients it will lead to an over- or underestimation of those parameters.

As mentioned before, the resolution needs to be high in order to segment the cartilage correctly. Moreover, the parameters need to be calculated with the correct and known *b*-value. Hence, for DTI imaging of articular cartilage, eddy current calibration is of high importance.

Methods

Two methods were used to determine whether eddy currents were present. First, images were acquired with the highest gradient strength (TE/TR = 42/1500 ms, Matrix = 256×256, in-plane resolution = 0.6×0.6 mm^2, 100 spokes, G = 39 mT/m, slew rate = 100 mT/m/s, slice thickness = 3 mm, b=400 s/mm^2, Δ = 25 ms, δ = 16 ms) on a water phantom with the diffusion directions used for DTI in opposite polarizations (12 measurements). To evaluate whether geometric distortions are present, several slices were segmented. For each slice, the segmentations for the six different diffusion gradient directions were overlaid as illustrated in Fig. 16. The different colors represent the different diffusion gradient directions. The boxes show magnifications of the overlaid segmentations. The error between the individual segmentations was then calculated with Matlab (MathWorks, Natick, Mass).

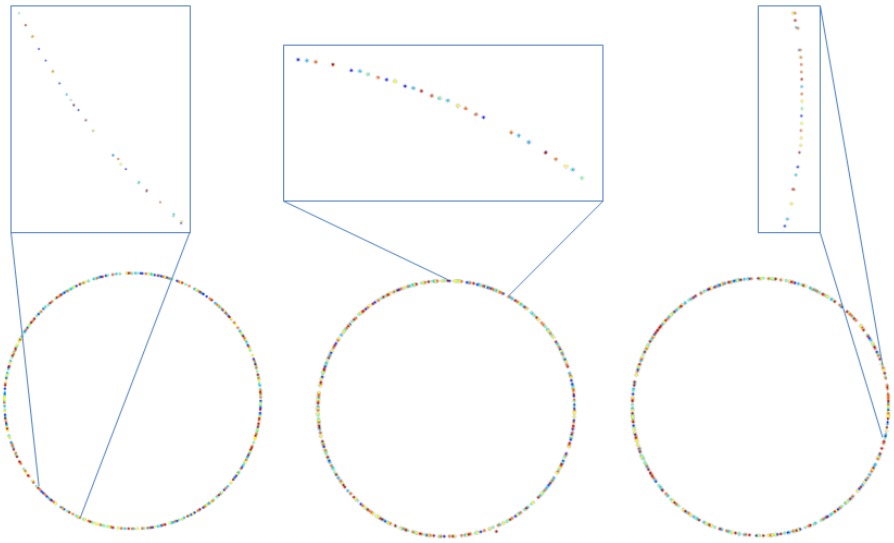

Figure 16: Segmentation of three slices. The colors indicate segmentations with different gradient directions. In boxes are presented magnifications of segmentations to show details

Afterwards, images of a different water phantom, consisting of three water bottles, were acquired in one direction and its inversed direction (+Readout and –Readout) with different gradient strengths (15 mT/m, 20 mT/m, 25 mT/m, 30 mT/m, 35 mT/m, 39 mT/m). In Matlab a mask was generated where each water bottle was assigned to a different number (indicated by the different colors in Fig. 17).

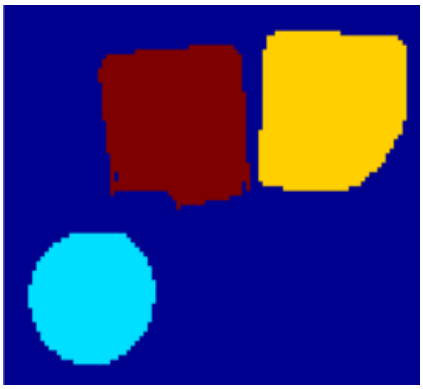

Figure 17: Mask of water phantom, consisting of three bottles (colors indicate each different phantom)

With the mask, the differences in intensity between +Readout (+RO) and –Readout (-RO) were calculated separately for each phantom. Then the relative difference between +RO and –RO and the standard deviation could be calculated, which is illustrated in Fig. 18. Each color (blue, green and red) represent one of the water bottles.

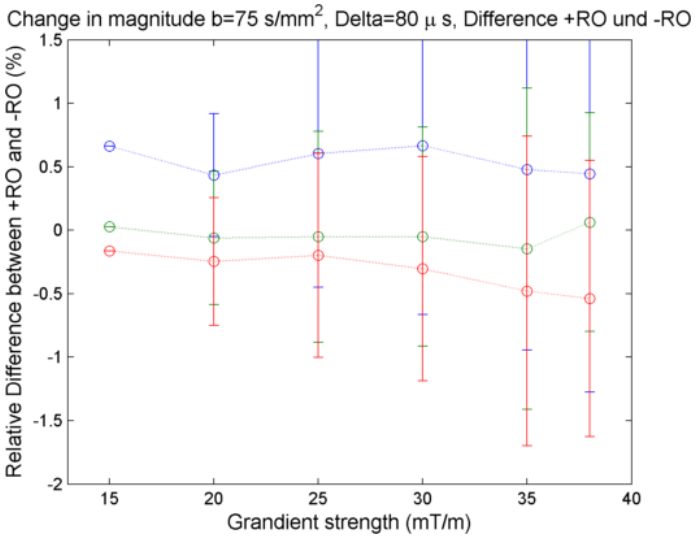

Figure 18: Relative difference in % between the signal intensity acquired with the diffusion gradients in the +Readout direction and the –Readout direction for different gradient strengths (15 to 39 mT/m)

Results

Fig. 16 shows the good agreement of the segmentations performed on images with different diffusion gradients. Quantification of the segmentation errors demonstrated an error lower than 10% of the voxel size (*i.e.* 0.6 mm), which is comparable to the test retest error of the segmentation algorithm [115].

Fig. 18 illustrates the relative difference between the two directions for each gradient strength for all three phantoms (red, green and blue). The difference is rather small with a maximum difference of less than 1% and comparable with the error in two consecutive measurements without the same orientation of the diffusion gradients.

Conclusion

The experiments did not demonstrate any evidence of eddy currents.

5.2 Linearity of the diffusion decay

With an increase of the *b*-value the signal intensity should decay linearly. The same phantom as before, consisting of three water bottles, was scanned with six different *b*-values. The *b*-values were 75 s/mm^2, 150 s/mm^2, 225 s/mm^2, 300 s/mm^2, 375 s/mm^2 and 450 s/mm^2. The maximum gradient strength was 35 mT/m, the pulse duration δ 17 ms and the diffusion time Δ 24 ms. The logarithm of the signal intensity was then plotted against the *b*-value to

determine whether a linear decay was present (Fig. 19). The dots in Fig. 19 represent the logarithmic values of the signal intensity and the three solid lines represent the curve fitting for each phantom.

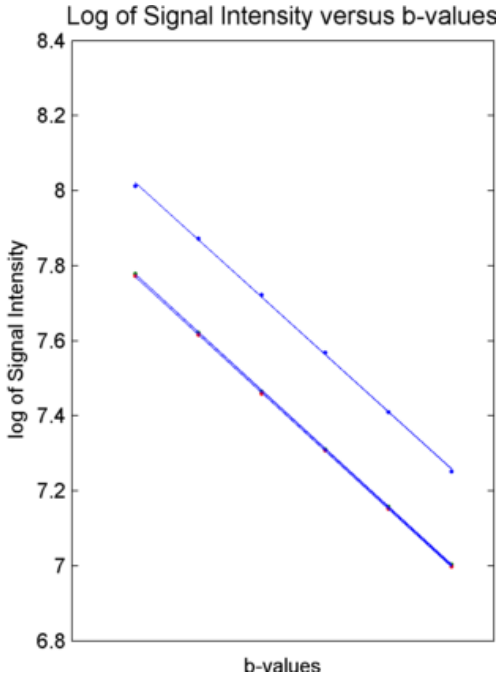

Figure 19: Plot of decaying signal intensity with increasing *b*-value

Conclusion

The signal decays linearly with increasing *b*-value.

5.3 Temperature dependent diffusivity

The ADC is temperature dependent, so that this dependence can be used as a calibration of the diffusion measurements. As the temperature increases, so does the ADC. We measured the mean diffusion coefficient in water phantoms at different room temperatures using the RAISED sequence (TR/TE = 38/1500 ms, in-plane resolution = 0.6×0.6 mm^2, matrix = 256×256, slice thickness = 3 mm, *b*-values = 400 s/mm^2, 1 direction readout, Δ = 20 ms, δ = 16 ms, slew rate = 100 mT/m/ms, bandwidth = 290 Hz/Pixel). The ADC measured with the RAISED sequence was compared to the data from the literature (Table 1) [116]. Our results demonstrated an average error of (-0.4±1.7)%.

T in °C	measured ADC in units of 10^{-3} mm^2/s	expected ADC in units of 10^{-3} mm^2/s	Relative error in %
15.3	1.8	1.8	2.6
18.8	2.0	2.0	0.7
18.8	2.0	2.0	0.9
20.3	2.0	2.0	-1.2
20.8	2.0	2.1	-0.8
21.1	2.0	2.1	-3.0
21.3	2.0	2.1	-1.8
21.3	2.0	2.1	-1.7
21.5	2.1	2.1	-0.7
21.7	2.1	2.1	1.0

Table 1: Mean diffusivity of measured data in water at different temperatures, values from literature and the relative error.

The measured mean diffusivity and the expected mean diffusivity showed excellent correlation (r^2=0.96, P<0.001). Fig. 20 illustrates the measured mean ADC values at the different temperatures (circles) and the theory curve of what the increase in ADC should look like with increasing temperature (solid line). As seen in Fig. 20, the ADC increases with an increase in temperature, agreeing well with the theory.

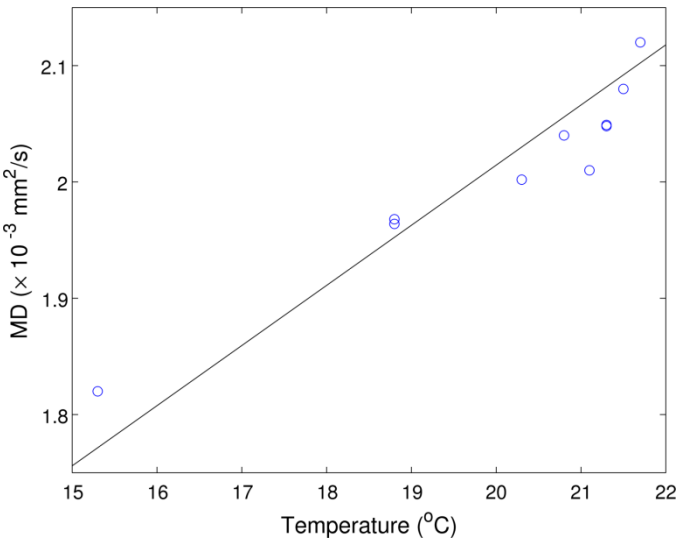

Figure 20: Plot of measured mean ADC against temperature (circles) and theory curve (solid line)

Conclusion

The diffusion values acquired with the RAISED sequence are in excellent agreement with the data published in the literature. These results provide additional evidence of the small effect of eddy currents in our measurements.

5.4 Comparison with Cartesian sequence

The following experiments were devoted to testing whether the radial acquisition introduces any artifacts as compared to the Cartesian acquisition. Images were acquired with the radial sequence and the parameter maps compared to the ones obtained with a Cartesian sequence. Aside from the *k*-space sampling the sequences have exactly the same parameters (TR/TE=50/1200 ms, in-plane resolution = 0.6×0.6 mm^2, slice thickness = 2 mm, *b*-values = 500 s/mm^2, 1 direction readout, Δ = 25 ms, δ = 19 ms, slew rate = 100 mT/m/ms, bandwidth = 381 Hz/Pixel), both the RAISED and the Cartesian images have the same matrix and similar acquisition times (Cartesian: encodings = 160, acquisition time = 3:12 min ; RAISED: spokes = 251, acquisition time = 5:01 min)

Asparagus was used as a phantom. The asparagus stems were stacked into a plastic container, which was then filled with water. Asparagus predominately consists of water and also has highly organized fibers along the stem with thick walls. These fibers restrict the motion of the water molecules and cause anisotropic diffusion, which makes it valuable for diffusion imaging.

An image with a *b*-value of zero and an image with a *b*-value of 500 s/mm^2 were acquired. The ADC map was calculated with the non-weighted and the diffusion-weighted image. Fig. 21 shows the ADC maps of the asparagus phantom derived from the radial data and the Cartesian data. On the maps, one can clearly see the free water with higher ADC values (orange to red color) around the stacked asparagus stems and the round asparagus stems with the lower ADC values (blue to yellow color). The lower image quality (blurring) in the Cartesian sequence could be due to motion artifacts caused by the vibration of the patient table during data acquisition.

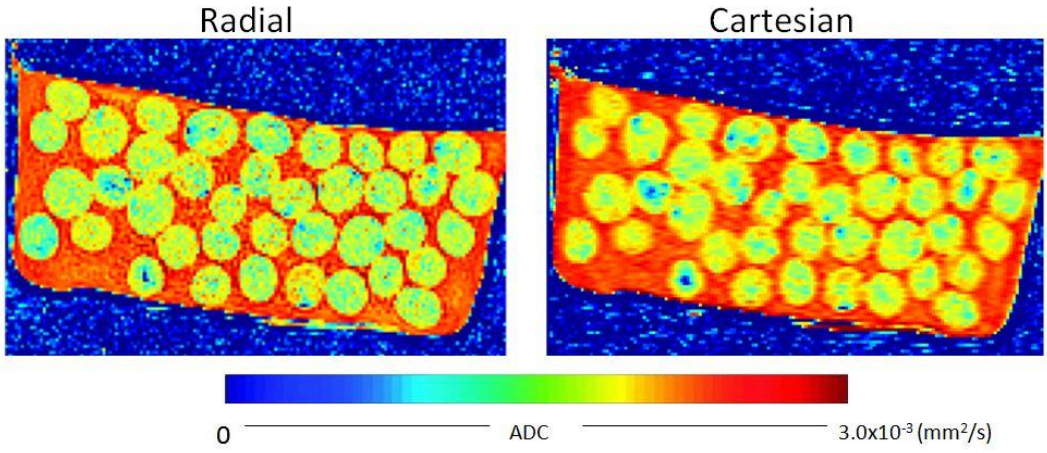

Figure 21: ADC maps of asparagus phantom

Mean ADC values were calculated in free water and in asparagus for the radial and Cartesian data. For the radial data, a mean ADC of (2.3±0.1)×10^{-3} mm^2/s in free water and of (1.7±0.2)×10^{-3} mm^2/s in asparagus was calculated and for the Cartesian data the mean ADC was calculated as (2.4±0.1)×10^{-3} mm^2/s in free water and (1.7±0.1)×10^{-3} mm^2/s in asparagus. The difference of the ADC measured with the RAISED sequence in relation to the Cartesian sequence was 3% in water and 2.6% in asparagus.

Conclusion

Both the RAISED and the Cartesian sequences provided the same results and neither were affected by artifacts

5.5 Image acceleration

With the RAISED sequence, the full sampling of the *k*-space takes more than an hour. However, scan times over one hour are not clinically acceptable. Hence, the sequence needs to be accelerated. The goal is to reduce the scan time to less than 20 minutes.

A radial sequence is accelerated by reducing the number of spokes. However, reducing the number of spokes leads to streaking artifacts in the image. Therefore, it needs to be tested how the acceleration influences the image quality and the data quality. Images of a water phantom were acquired with the RAISED sequence (TR/TE=50/1200 ms, in-plane resolution = 0.6×0.6 mm^2, matrix = 128×128, slice thickness = 2 mm, *b*-values = 400 s/mm^2, 1 direction readout, Δ = 25 ms, δ = 19 ms, slew rate = 100 mT/m/ms, bandwidth = 381 Hz/Pixel) with fully sampled *k*-space (spokes = 201; acquisition time = 4:01 min), an undersampling ratio of 2 (one each two lines, spokes = 101, acquisition

time = 2:01 min) and 3 (spokes = 67, acquisition time = 1:20 min). The ADC maps were then calculated (Fig. 22).

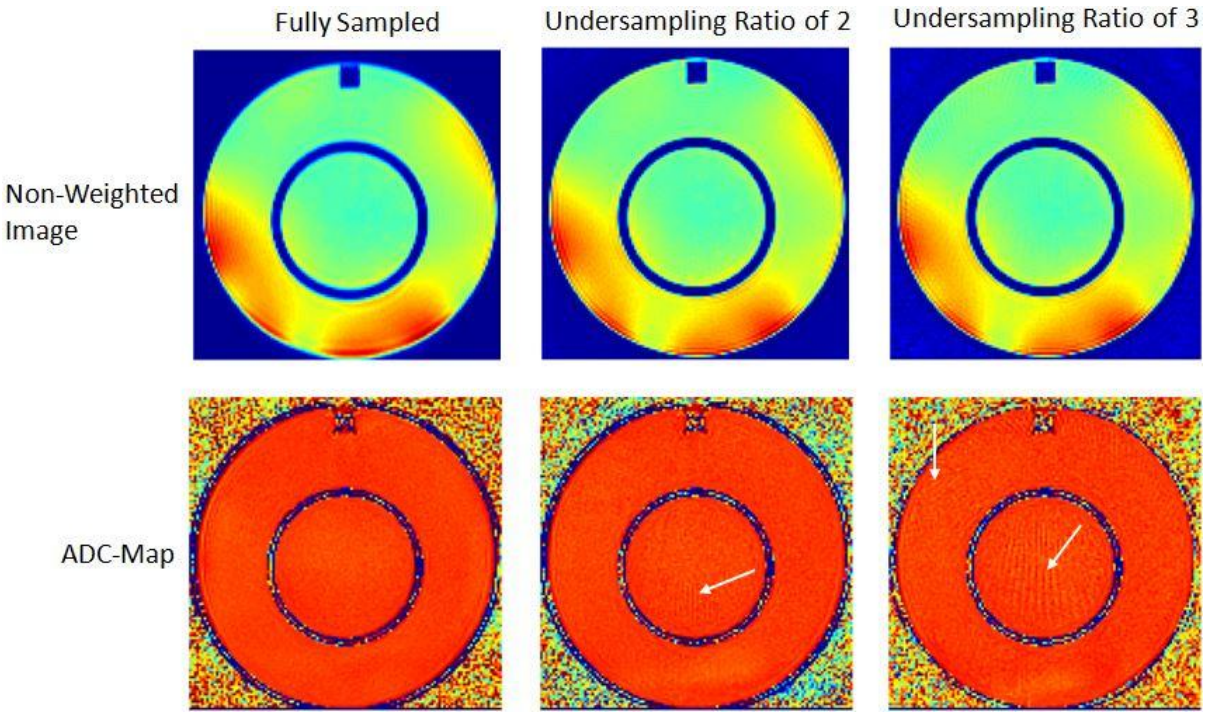

Figure 22: Non-weighted images and ADC maps acquired with full sampling, undersampling ratio of 2 and undersampling ratio of 3. The black arrows point out the streaking artifacts in the undersampled images.

The mean ADC measured with all acquisitions was calculated as 2.4×10^{-3} mm^2/s. Hence, the mean ADC stayed the same irrespectively of the acceleration factor. However, the standard deviation of the ADC slowly increased from 0.4×10^{-3} mm^2/s at no acceleration to 0.6×10^{-3} mm^2/s at an acceleration factor of 2, and to 0.8×10^{-3} mm^2/s at an acceleration factor of 3. As expected, the noise increased with higher acceleration and so did the amount of streaking artifacts (black arrows in Fig. 22).

In addition to the experiments on a water phantom we performed experiments on an asparagus phantom to test the effect of acceleration in the FA. Images were acquired using the RAISED sequence (TR/TE = 45/1500 ms, in-plane resolution = 1.2×1.2 mm^2, matrix = 224×224, slice thickness = 3 mm, b-value = 350 s/mm^2, Δ = 21 ms, δ = 16 ms, slew rate = 100 mT/m/ms, bandwidth = 381 Hz/Pixel) with an acceleration factor of 1 (spokes = 351, acquisition time = 8:47 min) and an acceleration factor of 3 (spokes = 114; acquisition = 2:51 min). Diffusion-weighted images were acquired in six directions. The diffusion tensor was calculated, hence the MD and FA maps (Fig. 23).

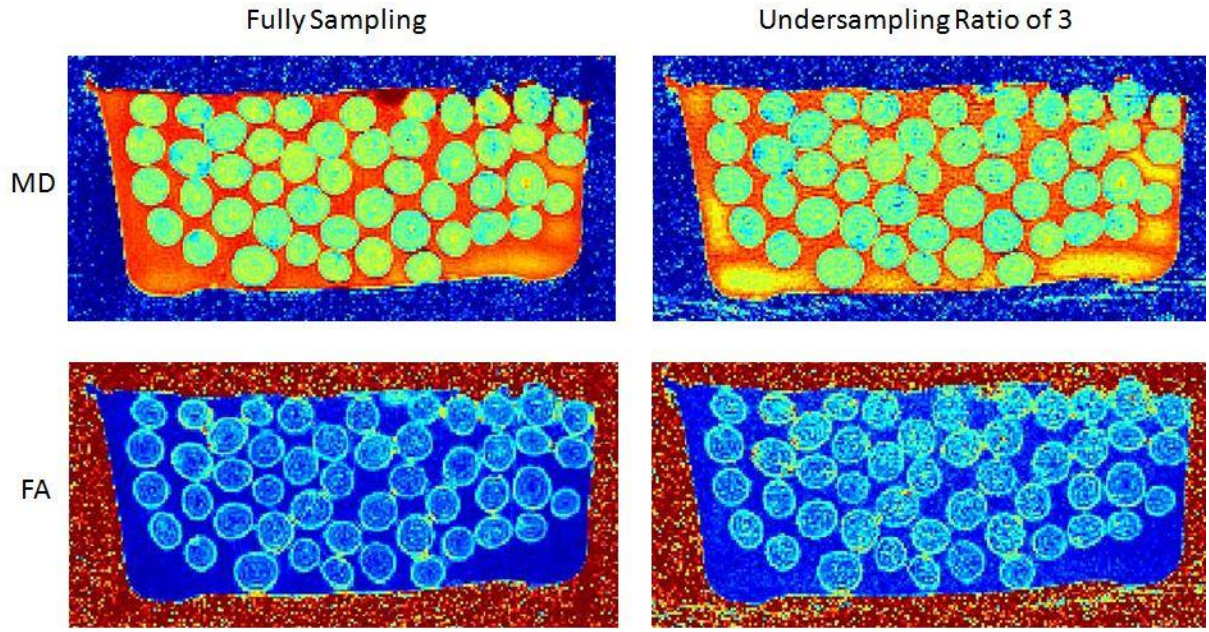

Figure 23: MD and FA maps of asparagus phantom for fully sampling and for an acceleration factor of 3

In Fig. 23, the differences in FA show better contrast in the asparagus stems in the fully sampled images. This is most likely due to the lower SNR in the accelerated image, which caused an increase in FA. The mean MD in water was calculated as (2.4±0.1) $\times 10^{-3}$ mm^2/s for full sampling and undersampling with a resulting coefficient of variation (standard deviation divided by mean) of 3.3% for full sampling and 5% for undersampling. The mean MD in asparagus was (1.5±0.1)$\times 10^{-3}$ mm^2/s for full sampling and (1.5±0.2)$\times 10^{-3}$ mm^2/s with acceleration which resulted in a coefficient of variation of 6.7% and 13.3% for the fully sampled and the accelerated images respectively. The mean FA in water without acceleration was (0.08±0.03) and (0.12±0.05) for an acceleration of 3. This leads to a coefficient of variation of 33.7% for full sampling and 38.8% for undersampling. In asparagus the mean FA was calculated as (0.21±0.06) with no acceleration and (0.26±0.08) with acceleration. Hence, the coefficients of variation were 29.7% and 31.9% without acceleration and with acceleration respectively.

Conclusion

The images of the water phantom acquired with the accelerated sequence presented streaking artifacts. However, the images of the asparagus phantom did not show any streaking artifacts. Furthermore, those artifacts are low in signal and can be compensated. Accelerating the sequence did not have an impact on the mean MD. The values were the

same for the full sampling and the undersampling. As expected, the coefficient of variation was higher in the accelerated image due to the higher noise in accelerated images. The mean FA also showed increased values in the accelerated data. This is most likely due to the lower SNR in the accelerated images as FA is known to be very sensitive to SNR. However, SNR can be increased by protocol optimization. To allow for good parameter calculation, the protocol has to be optimized and tested in human subjects, which will be explored in chapter 6. Hence, the acquisition can be accelerated to have acquisition times compatible with clinical scans.

5.6 Reconstruction

As demonstrated in earlier chapters, accelerating radial sequences leads to additional noise and streaking artifacts. This may present problems for the diagnosis of the patients. It is therefore of high importance to reduce these artifacts to a minimum. Images of a knee with the RAISED sequence (TR/TE = 45/1500 ms, in-plane resolution = 0.75×0.75 mm^2, matrix = 208×208 slice thickness = 3 mm, 1 direction readout, slew rate = 100 mT/m/ms, bandwidth = 394 Hz/Pixel) and an undersampling ratio of 3 (spokes = 114, acquisition time = 2:51 min) were acquired. A plastic tube filled with water was placed underneath the knee. The images were then reconstructed using a conventional gridding and an iterative reconstruction algorithm as explained in chapter 4. In Fig. 24 the two images are illustrated. The white arrows point out streaking artifacts.

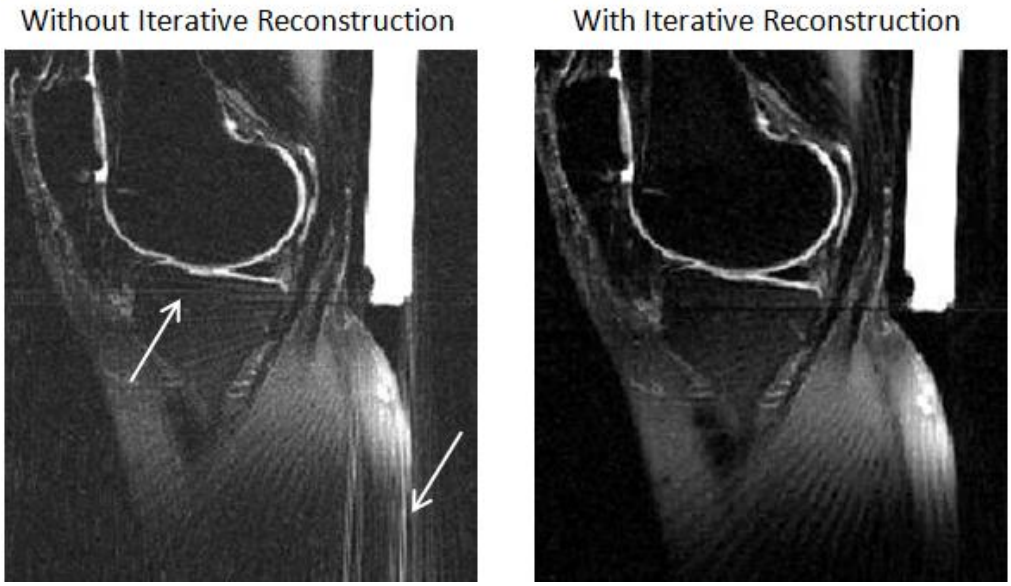

Figure 24: MR image of knee, reconstructed with a conventional gridding and with an iterative reconstruction algorithm. The white arrows point out streaking artifacts.

The iterative reconstructed image exhibits less noise (Fig. 24). Moreover, the streaking artifacts are reduced. Nevertheless, a significant drawback of this method is the longer reconstruction time of approx. 20 min/slice compared to the approx 3 s/slice for conventional gridding.

Conclusion

The iterative reconstruction algorithm reduced the streaking artifacts and the noise in the image. However, the reconstruction time is very long and requires off-line reconstruction. As our final protocol (see chapter 6) was not affected by streaking artifacts, we did not need to use iterative reconstruction and used the conventional gridding algorithm implemented in the scanner.

5.7 Signal-to-Noise Ratio

One of the most important parameters to measure the image quality is the so-called signal-to-noise ratio (SNR). It describes the relationship between the intensity of the MR signal and its noise. A higher SNR is desirable for accurate measurement of diffusion parameters. The image SNR depends on several pulse sequence parameters: the number of averages, the slice thickness, the field of view (FOV), the bandwidth, the echo time and the matrix size. By changing these parameters, the SNR can be increased. However, in order to increase SNR,

parameters such as the echo time or the resolution have to be changed. Hence, these parameters have to be optimized carefully to find the best compromise (see chapter 6).

Images of a water phantom were acquired with the RAISED sequence and a Cartesian sequence to compare the SNR of both images using the same protocol as described in section 5.5 for the water phantom. The SNR maps were calculated for both the radial and the Cartesian sequence by fitting the background distribution to a Rician distribution (Fig. 25).

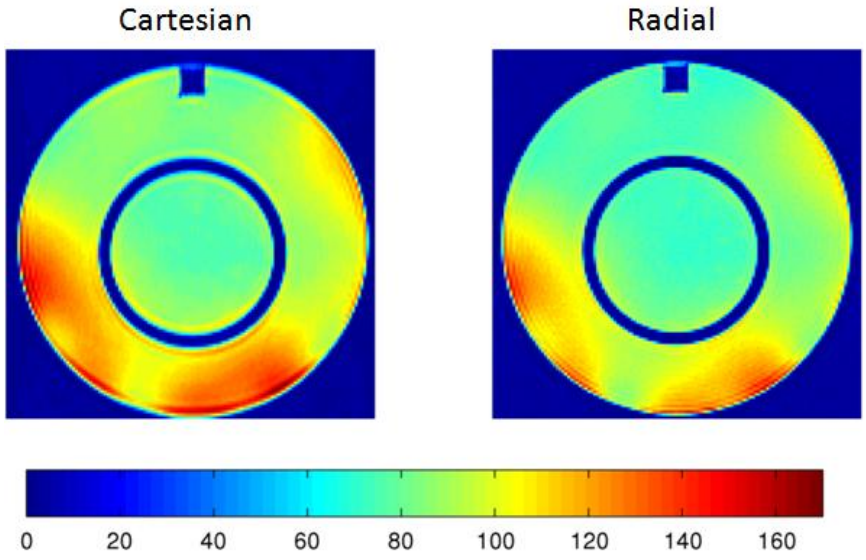

Figure 25: SNR maps of water phantom acquired with Cartesian and radial sequence

The mean SNR derived from the Cartesian data was calculated as 93±23 and the mean SNR derived from the radial data was calculated as 92±18.

Conclusion

The difference in mean SNR between the Cartesian and the RAISED sequence was 1.1%. Hence, the RAISED sequence demonstrated equal image quality to the Cartesian sequence.

Summary of Chapter 5

The calibration of the RAISED sequence with the help of water and asparagus phantoms showed promising results for its *in vivo* application. The comparison with the conventional Cartesian sequence provided the same results for both Cartesian and radial data. It was also demonstrated that the RAISED sequence can be accelerated in order to reduce scan time for clinical routine. However, the sequence also needs to be optimized and tested in human subjects before it can be used in clinical scans.

6. Protocol optimization for *in vivo* DTI of articular cartilage

For the correct calculation of the diffusion parameters, a protocol that provides enough SNR at high *b*-values is required. However, additionally the measuring time needs to be kept within 20 minutes. Thus, the protocol for the RAISED sequence has to be optimized.

6.1 Protocol optimization

As a reference protocol, the protocol with fully sampled radial *k*-space was considered (TR = 1500 ms, TE = 49 ms, spokes = 402, matrix = 256×256, FOV = 154 mm^2, slice thickness =3 mm, acquisition time = 70:21 min, in-plane resolution = 0.6x0.6 mm^2). A healthy volunteer was scanned with a fully sampled acquisition and five slices were acquired. A whole diffusion tensor measurement was performed with six diffusion directions (see chapter 4). Diffusion-weighted images were acquired with a *b*-value of 400 s/mm^2. This protocol has an acquisition time of 1:10 hours and resulted in excellent image quality and sufficient SNR for the diffusion parameter calculation in the diffusion-weighted images (Fig. 26).

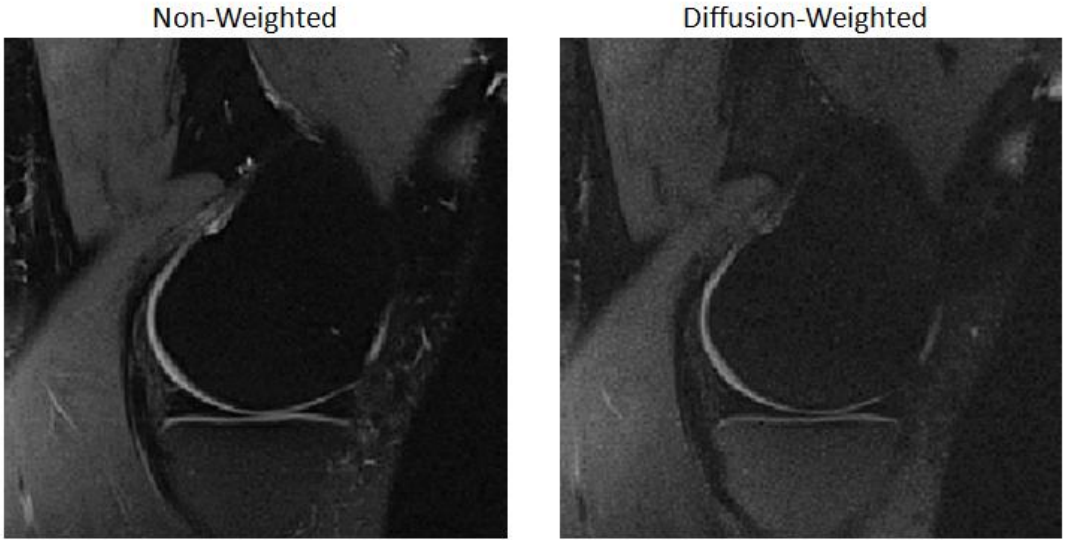

Figure 26: Fully sampled images of a healthy subject with and without diffusion weighting

The objective was to establish a protocol that results in the same SNR, but with a significant reduction of the acquisition time as scan times longer than 20 minutes are not applicable for clinical scans. This was done by theoretical optimization of the reference protocol (Table 2). The resolution and the *b*-value were reduced in order to win signal and reduce the echo time. The relative SNR of the new protocol as compared to the fully sampled protocol was calculated as follows:

$$\frac{SNR_2}{SNR_1} = \frac{\Delta x_1 \cdot \Delta y_1 \cdot \Delta z_1}{\Delta x_2 \cdot \Delta y_2 \cdot \Delta z_2} e^{\frac{(TE_1 - TE_2)}{T2}} \times e^{(b_1 - b_2)D} \times \frac{(1 - e^{\frac{TR_2}{T_1}})}{(1 - e^{\frac{TR_1}{T_1}})} \times \sqrt{\frac{N_{Spokes2}}{N_{Spokes1}}} \quad (6.0)$$

where SNR_1 is the SNR of the original protocol and SNR_2 the SNR of the new protocol. TE represents the echo time, *b* the *b*-value, TR the repetition time, N_{Spokes} is the number of spokes, and Δx, Δy, Δz are the dimensions of the voxel. The subindex 1 indicates the parameters of the reference protocol and subindex 2 indicates the parameters of the new protocol. In this calculation we assumed a constant bandwidth and typical values in articular cartilage for T_1 (800 ms), T_2 (30 ms) and the diffusion constant (1×10^{-3} mm^2/s). The acquisition time was calculated for a full DTI acquisition (*i.e.* one unweighted and six diffusion-weighted images). The results are illustrated in the following table. In addition to the reference protocol (Protocol R), two protocols (Protocol A and Protocol B) were established. To reduce the scan time for the protocols to the goal of 20 minutes, different undersampling ratios (R) were considered.

	Protocol R			**Protocol A**			**Protocol B**		
	R=1	R=2	R=3	R=1	R=2	R=3	R=1	R=2	R=3
TR(s)	1.5	1.5	1.5	1.5	1.5	1.5	1.5	1.5	1.5
Resolution (mm)	0.6	0.6	0.6	0.7	0.7	0.7	0.75	0.75	0.75
N_{Spokes}	402	201	134	352	176	117	327	163	114
Base Resolution	256	256	256	224	224	224	208	208	208
FOV (mm^2)	154	154	154	157	157	157	156	156	156
b (s/mm^2)	400	400	400	350	350	350	350	350	350
TE (ms)	49	49	49	45	45	45	45	45	45
T_{acq} (min)	70:21	35:10	23:27	61:36	30:48	20:28	57:13	28:31	19:57
SNR_{rel}	1	0.71	0.58	1.53	1.08	0.88	1.69	1.20	1.00

Table 2: Tables of parameters for optimization of protocol

The gain/loss of relative SNR had to be calculated for each changed parameter using Eq. 6.0, *e.g.* if the echo time is reduced or increased the signal gain/loss is calculated as follows:

$$\frac{SNR_2}{SNR_1} = \frac{e^{-\frac{TE_2}{T_2}}}{e^{-\frac{TE_1}{T_2}}} \quad (6.1)$$

Table 2 shows that accelerating Protocol R with a factor of 3 to reduce the acquisition time to less than 20 minutes resulted in a SNR loss of 42%. Hence, the SNR needed to be improved by changing sequence parameters. It was first attempted to reduce the resolution from

0.6 mm to 0.7 mm and the diffusion weighting from a *b*-value of 400 s/mm^2 to a *b*-value of 350 s/mm^2 (Protocol A in Table 2). Furthermore, the echo time was reduced from 49 ms to 45 ms. Reducing the echo time results in higher signal and less T_2-weighting. Accelerating Protocol A with an undersampling ratio of 3 still resulted in a SNR loss of 12%. The resolution was further reduced from 0.7 mm to 0.75 mm (Protocol B in Table 2). Accelerating Protocol B with an undersampling ratio of 3 did not result in SNR loss. Protocol R, Protocol A and Protocol B were tested *in vivo* with an acceleration factor of 3 and based on these experiments the optimal protocol was determined (see chapter 6.2)

6.2 Protocol test *in vivo*

In order to determine which protocol was the optimal one, images of one subject were acquired with the three protocols from Table 2 (Protocol R, Protocol A, and Protocol B) and an undersampling ratio of 3 (Fig. 27)

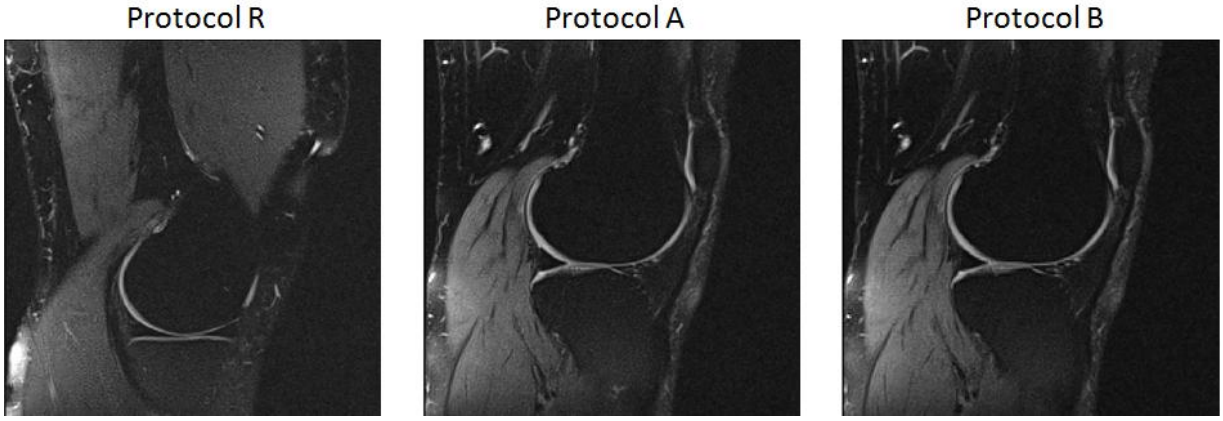

Figure 27: Images of the knee of the same subject acquired with the three protocols (Protocol R, Protocol A and Protocol B) and an undersampling ratio of 3

The image of Protocol R in Fig. 27 shows low SNR with an SNR below 15. This results in a high risk for the calculation of the FA to be biased, especially in the deeper zones of the articular cartilage due to their lower T_2 values and thus lower SNR. While Protocol A and B provided similar results, the SNR with Protocol B was better and there was more signal in the cartilage which is important for the correct calculation of the diffusion parameters. For Protocol B the SNR in the cartilage was calculated as 30±3.1 in the images without diffusion weighting and 17.5±2.5 with diffusion weighting. The images were of excellent quality. Furthermore, the images showed clear contrast with the cartilage and the synovial fluid, which makes it possible to accurately segment the articular cartilage. Hence, Protocol B with an acceleration factor of 3 was determined to be the optimal protocol. However, a lack of

SNR could still be seen after scanning several subjects. Therefore, before OA patients were scanned the diffusion weighting was further reduced from a *b*-value of 350 s/mm^2 to a *b*-value of 300 s/mm^2 to receive the optimal signal.

Comparison with Cartesian

To make sure the radial acquisition did not introduce any artifacts to the diffusion parameters the MD values acquired with the RAISED sequence were compared to the MD values acquired with a Cartesian sequence. A volunteer was scanned with the RAISED sequence and a Cartesian sequence with the same protocol (Protocol B in Table 2) in one session. The RAISED sequence was undersampled with a ratio of 3 and both sequences had the same matrix size (Cartesian: encodings = 208, acquisition time = 5:12 min; RAISED: spokes = 114, acquisition time = 2:51min). The ADC maps of both datasets were calculated (Fig. 28).

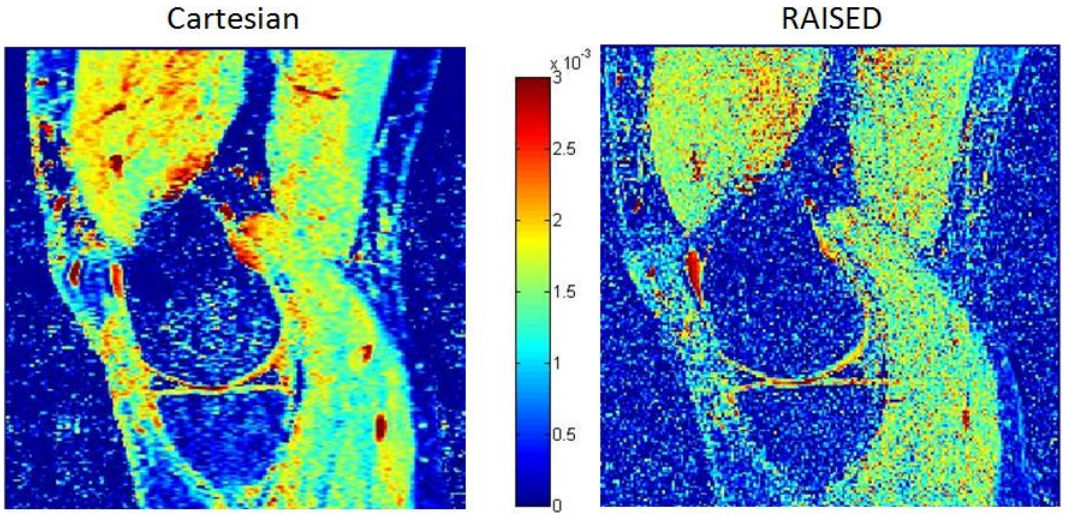

Figure 28: MD maps derived from Cartesian data and radial data in mm^2/s.

The mean MD for a section in the muscle was calculated for the Cartesian and radial data as (1.9±0.3)×10^{-3} mm^2/s and (1.8±0.4)×10^{-3} mm^2/s respectively.

Conclusion

The difference of the mean MD derived from the data acquired with the RAISED sequence in comparison to the Cartesian sequence was 5.6%. The difference in mean MD between the radial and the Cartesian sequence could be caused by motion during the acquisitions as Cartesian sequences are very sensitive to motion.

Summary of Chapter 6

The protocol B (Table 2) of the RAISED sequence presents high quality *in vivo* images of the knee with sufficient SNR for *in vivo* applications. The calculated diffusion parameters are comparable to the values acquired with Cartesian sequences. Hence, the sequence can now be validated at 3 T.

7. *In vivo* validation of RAISED sequence at 3 T

For the validation it was required to scan both healthy volunteers and OA patients. For the first clinical evaluation MR with the optimized RAISED sequence was performed on two healthy subjects (age 36±5 years) and three OA subjects (age 63±8 years). The three OA patients were Kellgren-Lawrence grade II.

7.1 Methods

The *in vivo* validation was performed on a 3 T scanner (MAGNETOM Skyra, Siemens AG). The optimized protocol was used to scan the subjects (optimal Protocol B in Table 2). Due to the low T_2 in cartilage the echo time had to be kept short. For the diffusion-weighted images, a maximum *b*-value of 300 s/mm^2 was used (diffusion time (Δ) = 21 ms, diffusion gradient duration (δ) = 16 ms). The reduced *b*-value made it possible to also reduce the echo time from 45 ms to 40 ms resulting in a SNR increase of 18%. For DTI, diffusion-weighted images in six different directions and one non-diffusion-weighted image were acquired with a total of 21 3 mm slices. All sequences were performed in the sagittal plane.

The RAISED images were reconstructed using gridding of the radial views to a Cartesian grid. The reconstruction was done by the MR scanner and the images saved in dicom format. Femoral and tibial cartilage were segmented on the non-diffusion weighted image with a semiautomatic in-house developed algorithm for sub-voxel segmentation [115]. The segmentations were overlaid with the MR imaging parameter maps which presented the MD and FA maps of only the cartilage regions. These maps could then be overlaid with the non-diffusion weighted images of the knee. From the RAISED images, the eigenvectors and eigenvalues (λ_1, λ_2, λ_3) of the diffusion tensor were calculated by using custom Matlab routines.

With the segmentations, the mean MD and the mean FA could be assessed for each cartilage region separately (medial tibia, lateral tibia, patella, trochlea, medial femoral condyle, lateral femoral condyle).

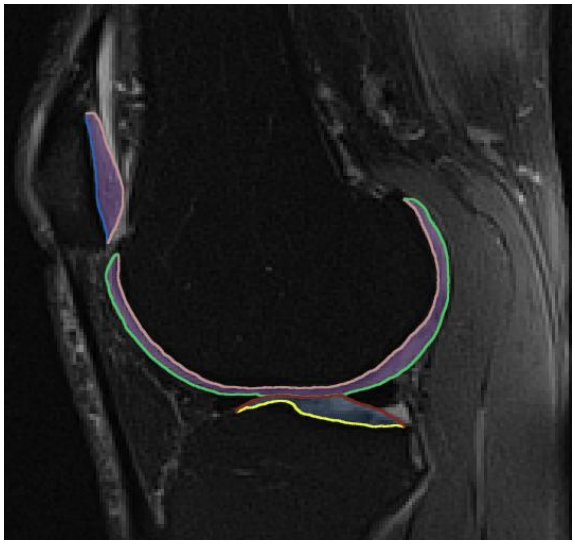

Figure 29: Image of knee with segmentations of the patellar (purple), femoral (purple) and tibial (blue) cartilage

Fig. 29 shows the segmentation of the cartilage with the algorithm for sub-voxel segmentation with the three cartilage regions of the tibia (blue), the femur (purple) and the patella (also purple).

The mean MD and FA were determined for both groups, the healthy volunteers and the OA patients.

Statistical Analysis

To determine whether there were significant differences present between the group of healthy volunteers and the group of OA patients, statistical analysis was preformed for each cartilage region. An unpaired two sided t-test was chosen with a significance level of 0.05 and conducted in Matlab. In order for a t-test to be applicable, the distributions of both groups have to be normal. The single-sample nonparametric Kolmogorov-Smirnov goodness-of-fit hypothesis test can determine whether a sample is normally distributed. The Kolmogorov-Smirnov test was performed for both the healthy group and the OA group for each cartilage region with Matlab.

For the Kolmogorov-Smirnov test the null hypothesis (H_0) states that the sample is normally distributed. The decision of the test is based on comparing the p-value and the chosen significance level, which is considered to be 0.05.

A null hypothesis also has to be stated for the t-test. H_0 says that there is no significant difference between the two tested groups, hence the healthy and the OA subjects. The decision of the test is based on comparing the p-value and the chosen significance level, which is, as before, considered to be 0.05.

7.2 Results

The results of the overlaying of the MD and FA maps with the non-weighted image are presented for the healthy subjects and the OA subjects in the following.

7.2.1 MD and FA Maps for healthy and OA subjects

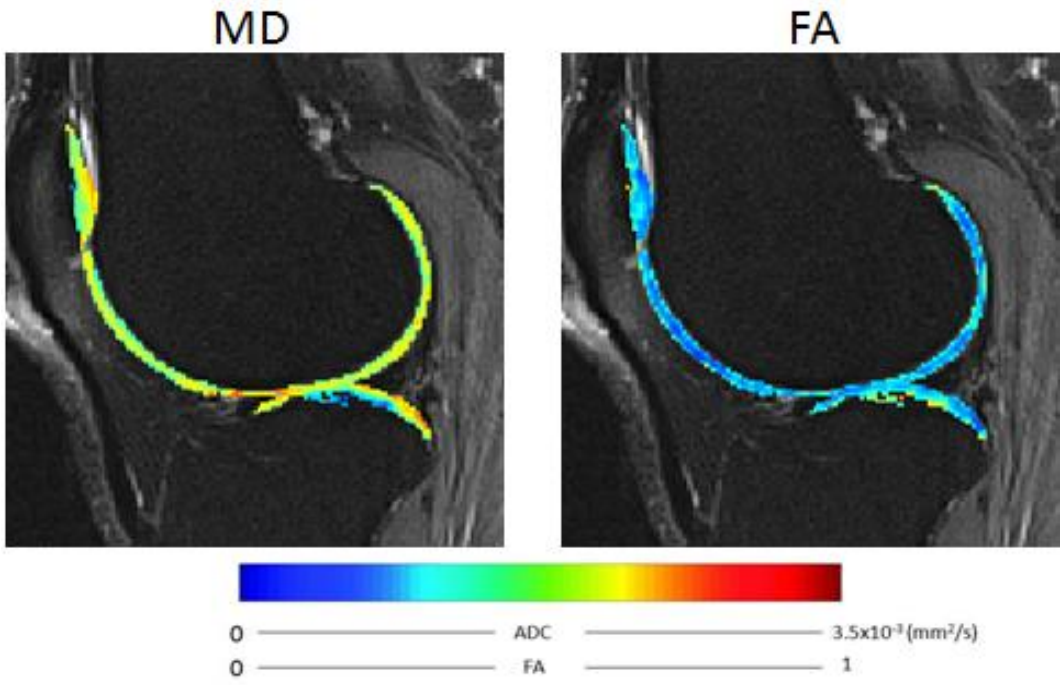

Figure 30: MD and FA maps of a healthy subject (H1)

Figs. 30 and 31 show the segmented MD and FA maps for the healthy volunteers.

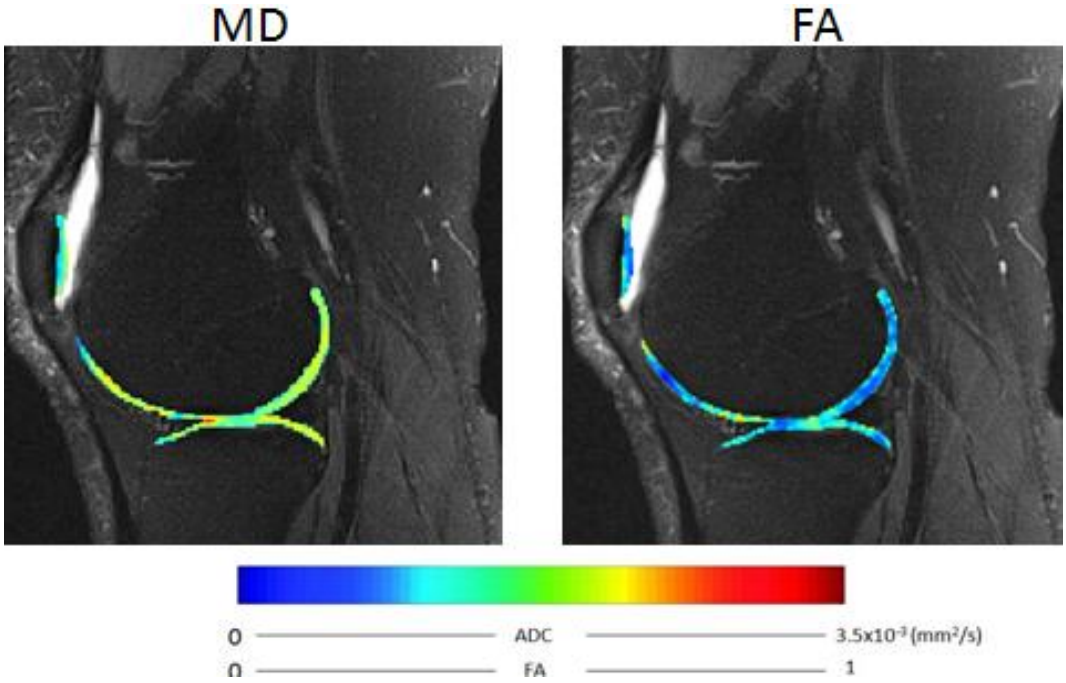

Figure 31: MD and FA maps of a healthy subject (H2)

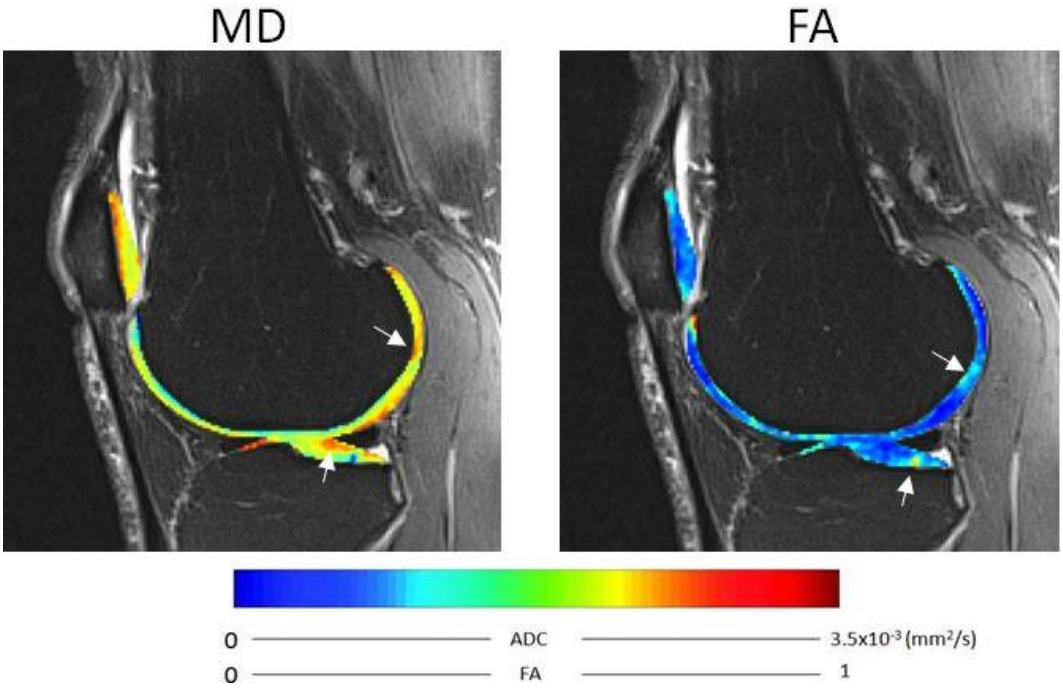

Figure 32: MD and FA maps of an OA patient (OA1). The white arrows indicate the increased MD and reduced FA in the lateral femoral condyle and the lateral tibia

The Figs. 32 to 34 show the result for the OA patients. Fig. 32 illustrates the results for the first OA subject. The white arrows point out increased MD and reduced FA in the lateral femoral condyle and the lateral tibia.

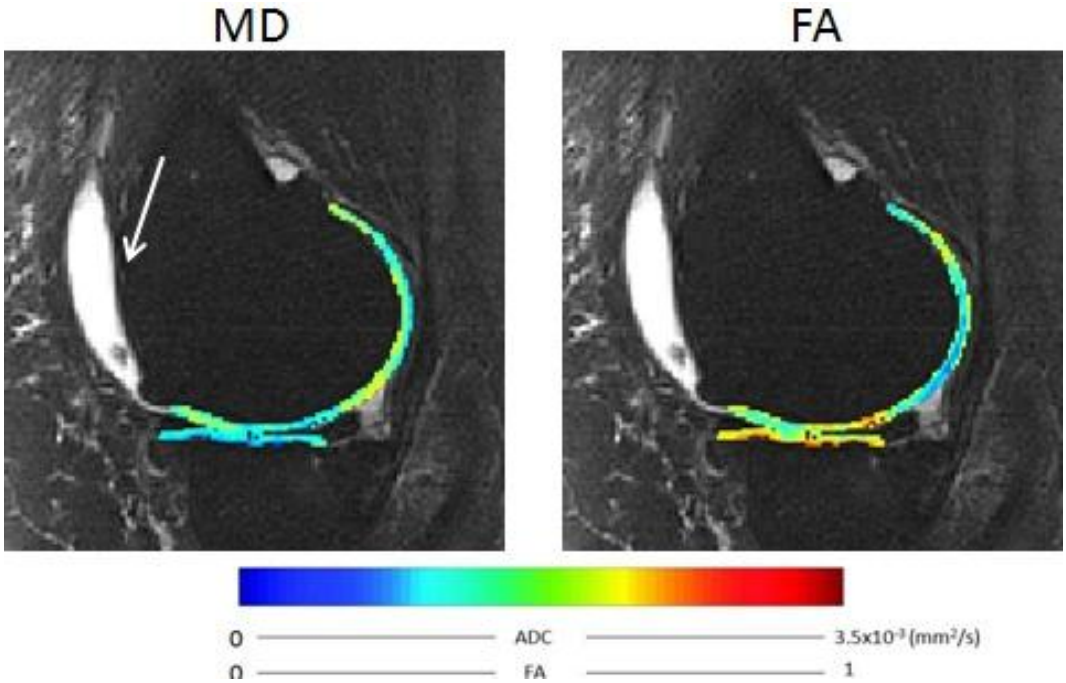

Figure 33: MD and FA maps of an OA patient (OA2). The arrow indicates joint effusion with abundant synovial fluid.

In Fig. 33 the results for the second OA subject are shown. It was not possible to segment the patella cartilage for this patient due to too much fluid in the knee, pointed out by the white arrow.

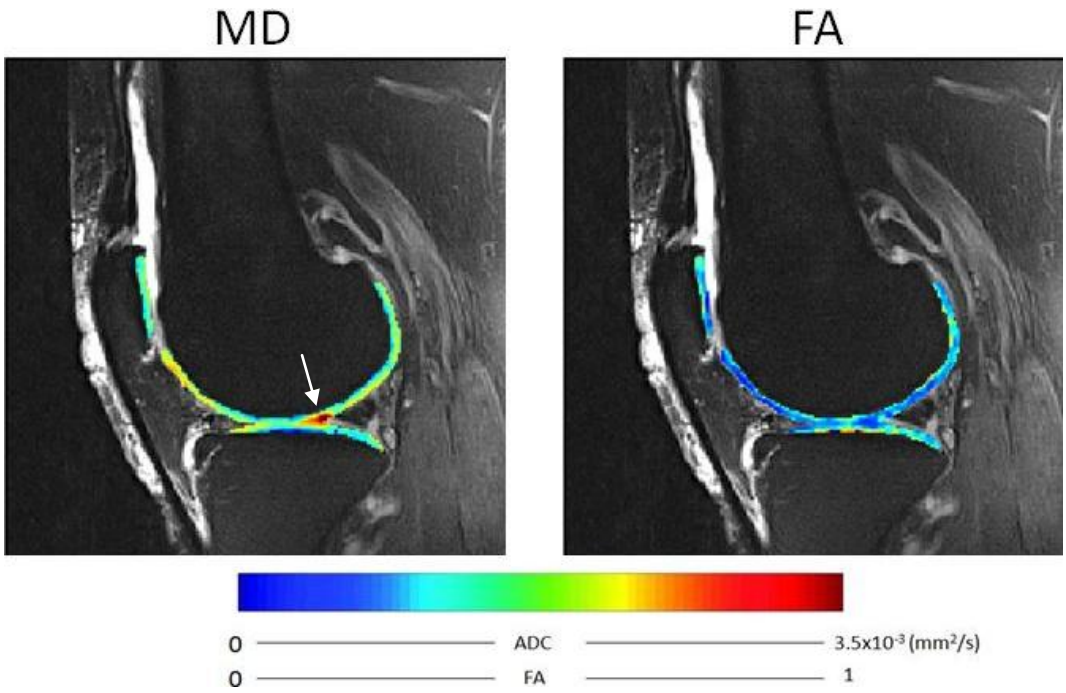

Figure 34: MD and FA maps of an OA patient (OA3). The white arrow indicates increased MD, most likely caused by fluid in the knee.

The high values in the MD map (white arrow) of OA subject 3 in Fig. 34 could be due to fluid in the knee.

7.2.2 Mean MD and mean FA in different cartilage regions

The mean MD in the different regions is summarized in Table 3:

Cartilage Region	H1	H2	OA1	OA2	OA3
Femur	2.1±0.4	1.9±0.5	2.1±0.8	1.8±0.4	2.1±0.7
Medial Tibia	2.1±0.6	1.7±0.5	1.9±0.7	1.6±0.6	2.4±0.9
Lateral Tibia	2.1±0.4	1.9±0.5	2.4±1.3	1.3±0.4	2.3±0.6
Patella	2.0±0.4	2.2±0.5	1.6±0.6	n/a	1.9±0.5

Table 3: Mean MD in different cartilage regions (in units of 10^{-3} mm^2/s) of the healthy volunteers (H) and the OA subjects (OA). n/a not available.

The mean FA in the different cartilage regions is summarized in Table 4:

Cartilage Region	H1	H2	OA1	OA2	OA3
Femur	0.46±0.18	0.35±0.16	0.43±0.18	0.40±0.15	0.35±0.16
Medial Tibia	0.50±0.18	0.43±0.18	0.46±0.17	0.51±0.18	0.40±0.15
Lateral Tibia	0.54±0.22	0.38±0.18	0.55±0.15	0.56±0.17	0.32±0.24
Patella	0.48±0.18	0.30±0.13	0.49±0.18	n/a	0.35±0.16

Table 4: Mean FA in the different cartilage regions of the healthy subjects (H) and the OA subjects (OA)

In one of the OA patients the patella in the cartilage could not be segmented due to fluid in the knee. The cartilage in the femur was then further divided into three more regions, the trochlea, the lateral femoral condyle and the medial femoral condyle as well as the mean MD and FA calculated. The mean MD of the different cartilage region in the femur is presented in Table 5.

Femur Region	H1	H2	OA1	OA2	OA3
Trochlea	1.9±0.3	2.0±0.6	1.9±0.6	1.7±0.5	1.9±0.6
Lat.Condyle	2.3±0.4	1.8±0.4	2.1±1.0	1.9±0.5	2.1±0.6
Med.Condyle	2.1±0.4	1.9±0.5	2.2±0.8	1.8±0.3	2.5±0.9

Table 5: Mean MD in the three different femoral regions (in units of 10^{-3} mm^2/s)

The mean FA values were determined for the three femoral compartments as follows:

Femur Region	H1	H2	OA1	OA2	OA3
Trochlea	0.41±0.15	0.32±0.15	0.39±0.14	0.47±0.16	0.32±0.14
Lat.Condyle	0.50±0.18	0.38±0.16	0.45±0.17	0.39±0.15	0.36±0.16
Med.Condyle	0.49±0.18	0.36±0.16	0.46±0.19	0.39±0.14	0.38±0.17

Table 6: Mean FA in the three different femoral regions

The MD and FA values showed no clear trend between the OA subjects and the healthy volunteers. However, two OA subjects had increased MD values in the lateral tibia and the lateral femoral condyle. Moreover, one subject showed reduced FA in the same two regions.

7.2.3 Statistical Analysis

The results for the Kolmogorov-Smirnov test for the mean MD values were as follows:

Cartilage Region	Healthy Group p-value	OA Group p-value
Femur	0,98	0,64
Med. Tibia	0,98	0,91
Lat. Tibia	0,98	0,72
Patella	0,98	0,98
Trochlea	0,98	0,64
Lat. Condyle	0,98	0,64
Med. Condyle	0,98	0,95

Table 7: Kolmogorov-Smirnov Test for the mean MD

For the mean MD all p-values are higher than the significance level of 0.05 (Table 7), thus all healthy and OA groups presented a normal distribution.

The same test had to be perfomed for the mean FA values. The following results were received:

Cartilage Region	Healthy Group p-value	OA Group p-value
Femur	0,98	0,91
Med. Tibia	0,98	0,97
Lat. Tibia	0,98	0,67
Patella	0,98	0,98
Trochlea	0,98	0,98
Lat. Condyle	0,98	0,89
Med. Condyle	0,98	0,75

Table 8: Kolmogorov-Smirnov Test for the mean FA

All sample groups for the mean FA values presented higher p-values than 0.05 for both the healthy groups as well as the OA groups (Table 8). Therefore, all the groups are normally distributed.

The Kolmogorov-Smirnov test showed that an unpaired two sided t-test can be applied as all groups presented a normal distribution. The t-test was also performed with Matlab. The results for the mean MD values were as follows:

Cartilage Region	p-value
Femur	1,00
Tibia med.	0,86
Tibia lat.	1,00
Patella	0,19
Trochlea	0,30
Lat.Condyle	0,94
Med.Condyle	0,58

Table 9: t-test results for mean MD values

Table 9 demonstrates that all the received p-values are higher than the significance level of 0.05. Hence, there is no significant difference between the healthy group and the OA group.

The FA was also tested for significant differences between the healthy group and the OA group for each cartilage region. The result of the test is presented in Table 10.

Cartilage Region	p-value
Femur	0,83
Tibia med.	0,87
Tibia lat.	0,90
Patella	0,82
Trochlea	0,69
Lat.Condyle	0,53
Med.Condyle	0,81

Table 10: t-test results for mean FA values

For the mean FA in the different cartilage regions, the p-values were also greater than the significance level. Hence, there was no significant difference between the healthy subjects and the OA patients detected for any of the cartilage region.

The t-test revealed no significant difference between the healthy volunteers and the OA patients. However, the sample sizes were quite small. Therefore, it is difficult to detect a significant difference. More subjects will need to be scanned in the future for further investigation.

7.3 Discussion

Testing the RAISED sequence at 3 T revealed excellent image quality and robustness against motion artifacts. The sequence validation with phantoms demonstrated the absence of eddy currents. It was also determined that the MD and FA values in water phantoms agreed well with data published in previous works. Moreover, the temperature dependent diffusivity coincided with the literature values. The comparison with the Cartesian spin echo acquisitions ascertained that the RAISED sequence was a good alternative with advantages over the Cartesian sequence, such as the robustness against motion artifacts and the possibility to accelerate the image acquisition to reduce the scan time.

The optimization of the protocol provided a protocol with sufficient SNR for correct diffusion parameter calculation. Obtaining a whole set of DTI data could be achieved in less than 20 minutes. The *in vivo* images showed excellent image quality and SNR above 15 so that an accurate calculation of the diffusion parameters was ensured. Moreover, the diffusion images have excellent contrast to segment the cartilage correctly. This is of high importance because the incorrect segmentation could lead to errors in the diffusion parameter assessment. Therefore, due to the sufficient SNR and the correct cartilage segmentation it was possible to derive accurate MD and FA from the DTI data acquired with the RAISED sequence.

The asparagus phantom tests showed that the data acquired with the RAISED and the Cartesian sequence resulted in the same ADC. It also showed that the accelerated sequence provided the same MD values as the fully sampled sequence in water as well as in asparagus. The mean FA and the coefficients of variation were higher in the accelerated images. However, this was most likely due to the lower SNR in the accelerated sequence. The protocol optimization increased the SNR for correct parameter estimation.

The *in vivo* tests demonstrated high quality diffusion-weighted images. The comparison with a Cartesian sequence showed that there was a difference in ADC of 5.6%. However, Cartesian sequences are very sensitive to motion so the difference could be caused by motion during the data acquisition.

Several studies published diffusion parameters for articular cartilage. Maroudas *et al.* provided the first values for healthy and OA cartilage when measuring a mean ADC of 1.30×10^{-3} mm^2/s in healthy cartilage and 1.45×10^{-3} mm^2/s in OA cartilage [93, 94]. Mlynárik *et al.* also measured an increased ADC in the range of 1.15×10^{-3} mm^2/s to 1.60×10^{-3} mm^2/s for

OA cartilage and 0.75×10^{-3} mm^2/s to 1.20×10^{-3} mm^2/s for healthy cartilage, although these experiments were performed *ex vivo* at 25 ˚C. The values published by Filidoro *et al.* for MD and FA in healthy cartilage were $(1.28\pm0.14)\times10^{-3}$ mm^2/s and (0.74±0.19), respectively. Several studies on artificial degradation of the macromolecules in the extracellular matrix supported the idea that a change in PG content is responsible for changes in the mean diffusivity (MD) and a change in the collagen network is responsible for changes in anisotropy (FA) [4, 77, 101]. Moreover, the correlation of DTI data with scanning electron microscopy (SEM) further proved the relationship between the collagen network and the anisotropy in cartilage [33, 100]. In good agreement, *in vivo* studies published show that in OA patients the average MD increases whereas the average FA decreases as compared to healthy cartilage [9, 77, 102].

In the first *in vivo* study of DTI measurements including healthy and OA subjects Raya *et al.* provided MD values in healthy volunteers in the range of $(0.75\pm0.31)\times10^{-3}$ mm^2/s to $(1.21\pm0.35)\times10^{-3}$ mm^2/s and FA values from (0.41±0.21) to (0.22±0.31). In healthy subjects the MD has a typical pattern of increasing values from the bone cartilage interface towards the articular surface, while the FA decrease from the bone cartilage interface to the articular surface. In OA subjects Raya *et al.* measured MD values from the bone-cartilage interface to the articular surface of $(1.01\pm0.32)\times10^{-3}$ mm^2/s and $(1.46\pm0.36)\times10^{-3}$ mm^2/s respectively and FA values of (0.31±0.18) and (0.21±0.17) [9]. In comparison, the MD and FA values that were measured in this work with the RAISED sequence in the cartilage were higher, with a mean MD in the whole cartilage of 2.0×10^{-3} mm^2/s for both the healthy and the OA subjects and a mean FA of 0.43 in healthy cartilage and 0.42 in OA cartilage. The increased values were present due to phase incoherence caused by microscopic motion between different acquisitions. A 2D phase navigator has been added to the sequence to correct for macroscopic motion and parameter maps after the phase correction showed MD and FA values in the range of the data published in the literature. Fig. 35 shows the MD and FA maps acquired with the RAISED sequence with and without 2D phase navigator. The decrease of the values is clearly visible, especially in the MD maps. The white arrows in Fig. 35 point out examples of lower valued areas as compared to the images without phase correction.

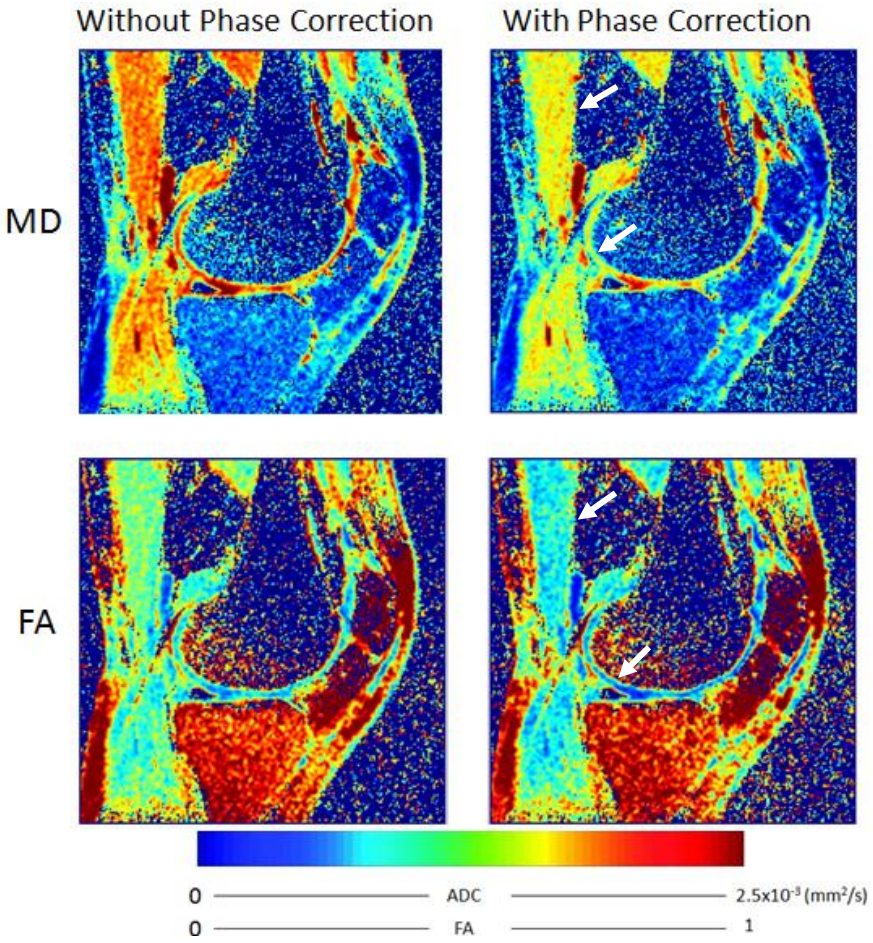

Figure 35: MD and FA maps before and after phase correction, with the white arrows indicating examples of lower MD and FA values in the phase corrected images as compared to the uncorrected images

Due to the small sample size of two healthy volunteers and three OA patients, no significant difference between the two groups could be determined. Hence, the increased MD and the decreased FA as suggested by the literature could not be seen in our data. A very likely cause of the lack of difference could be due to the scans being uncorrected from macroscopic motion. It is necessary to obtain more data from healthy and OA subjects to explore this further. Nevertheless, increased MD values were observed in two regions of the cartilage in two OA subjects and decreased FA in one subject in the same regions.

However, as of now DTI of articular cartilage was only possible at high field with high quality images. At 3 T, DTI of articular cartilage was previously done with EPI sequences, which led to low quality images [6-8]. The experiments presented in this work showed that with our RAISED sequence it was possible to acquire DTI images of excellent quality at 3 T which makes it applicable for clinical routine.

8. Conclusion and Outlook

OA is a big factor in industrialized countries due to its high prevalence and the absence of effective therapies. Not being able to diagnose OA in its early stages makes it difficult to develop new therapies. It is therefore of high importance to find a way to detect OA early. At high field, DTI of articular cartilage as a biomarker for OA has been proven to be very effective. However, high field scanners (>3T) are not allowed in clinical scanning. Hence, it is desirable to find a way to use DTI of articular cartilage as a biomarker for OA on clinical scanners as well. In this work I propose to use a spin echo radial (RAISED) sequence as we have proved that the RAISED sequence provides high quality images and is robust against motion artifacts. Moreover, it has been possible to obtain high quality DTI of articular cartilage at a 3 T scanner with an acquisition time below 20 minutes which makes the sequence usable in a clinical environment as well. We were first in providing high quality data of healthy and OA subjects at 3 T. The results of this work were selected as an e-poster at the annual meeting of The International Society for Magnetic Resonance in Medicine (ISMRM) [117]. Although data of a greater number of healthy and OA subjects need to be obtained, the results from this work are very promising. DTI of articular cartilage as a biomarker at 3 T could be of high importance for the detection of OA in its early stages in the future. Such early detection would ensure that the patients could start therapy early. Moreover, it may help to design trials for new OA drugs and to provide better understanding of the physiopathology of the disease. It would not only have a great positive impact on the individual patient, but also on industrialized countries as OA is a big burden on socioeconomics.

Bibliography

1. Braun, H.J. and G.E. Gold, *Diagnosis of osteoarthritis: Imaging.* Bone, 2012. **51**(2): p. 278-288.
2. Crema, M.D., et al., *Articular cartilage in the knee: current MR imaging techniques and applications in clinical practice and research.* Radiographics, 2011. **31**(1): p. 37-61.
3. Filidoro, L., et al., *High-resolution diffusion tensor imaging of human patellar cartilage: feasibility and preliminary findings.* Magn Reson Med, 2005. **53**(5): p. 993-998.
4. Meder, R., et al., *Diffusion tensor imaging of articular cartilage as a measure of tissue microstructure.* Osteoarthritis Cartilage, 2006. **14**(9): p. 875-881.
5. Raya, J.G., et al. *DTI of articular cartilage can predict early cartilage damage as assessed by histopathology*. in *20th conference of the International Society of Magnetic Resonance in the Medicine (ISMRM)* 2012. Melbourne, Australia.
6. Zhu, S.-C., D.-P. Shi, and A. Xuan, *Human patellar cartilage: echo planar diffusion-weighted MR imaging findings at 3.0 T.* Clinical Imaging, 2012. **36**(3): p. 199-202.
7. Xu, J., et al., *Value of T2-mapping and DWI in the diagnosis of early knee cartilage injury.* Journal of radiology case reports, 2011. **5**(2): p. 13.
8. Azuma, T., et al., *In vivo structural analysis of articular cartilage using diffusion tensor magnetic resonance imaging.* Magnetic resonance imaging, 2009. **27**(9): p. 1242-1248.
9. Raya, J.G., et al., *Articular cartilage: in vivo diffusion-tensor imaging.* Radiology, 2012. **262**(2): p. 550-559.
10. Horvai, A., *Anatomy and Histology of Cartilage*, in *Cartilage Imaging*. 2011, Springer. p. 1-10.
11. MMG, L.
12. Venn, M. and A. Maroudas, *Chemical composition and swelling of normal and osteoarthrotic femoral head cartilage. I. Chemical composition.* Ann Rheum Dis, 1977. **36**(2): p. 121-9.
13. Maroudas, A., M. Bayliss, and M. Venn, *Further studies on the composition of human femoral head cartilage.* Annals of the rheumatic diseases, 1980. **39**(5): p. 514-523.
14. Wang, C.C.-B., et al., *The functional environment of chondrocytes within cartilage subjected to compressive loading: a theoretical and experimental approach.* Biorheology, 2002. **39**(1): p. 11-25.
15. Raya, J.G., et al. *Multiparametric characterization of healthy and diseased articular cartilage at 17.6T: Comparison with histology.* in *17th congress of the International Society of the Magnetic Resonance in the Medicine (ISMRM)*. 2009. Honolulu, Hawaii, US.
16. BULLOUGH, P., *The distribution of collagen in human articular cartilage with some of its physiological implications.* 1970.
17. Clarke, I.C., *Articular cartilage: a review and scanning electron microscope study. 1. The interterritorial fibrillar architecture.* J Bone Joint Surg Br, 1971. **53**(4): p. 732-50.
18. Ratcliffe, A., P.R. Fryer, and T.E. Hardingham, *The distribution of aggregating proteoglycans in articular cartilage: comparison of quantitative immunoelectron microscopy with radioimmunoassay and biochemical analysis.* Journal of Histochemistry & Cytochemistry, 1984. **32**(2): p. 193.
19. Glaser, C. and R. Putz, *Functional anatomy of articular cartilage under compressive loading Quantitative aspects of global, local and zonal reactions of the collagenous network with respect to the surface integrity.* Osteoarthritis Cartilage, 2002. **10**(2): p. 83-99.
20. Kadler, K.E., A. Hill, and E.G. Canty-Laird, *Collagen fibrillogenesis: fibronectin, integrins, and minor collagens as organizers and nucleators.* Current opinion in cell biology, 2008. **20**(5): p. 495-501.
21. Wight, T.N., M.G. Kinsella, and E.E. Qwarnström, *The role of proteoglycans in cell adhesion, migration and proliferation.* Current opinion in cell biology, 1992. **4**(5): p. 793-801.

22. Bayliss, M.T., et al., *Sulfation of chondroitin sulfate in human articular cartilage.* Journal of Biological Chemistry, 1999. **274**(22): p. 15892-15900.
23. Knudson, C.B. and W. Knudson. *Cartilage proteoglycans*. 2001: Elsevier.
24. Buckwalter, J.A. and H.J. Mankin, *Articular cartilage: degeneration and osteoarthritis, repair, regeneration, and transplantation.* Instr Course Lect., 1998. **47:487-504.**
25. Aydelotte, M.B., R.R. Greenhill, and K.E. Kuettner, *Differences between sub-populations of cultured bovine articular chondrocytes. II. Proteoglycan metabolism.* Connective tissue research, 1988. **18**(3): p. 223-234.
26. Aydelotte, M.B. and K.E. Kuettner, *Differences between sub-populations of cultured bovine articular chondrocytes. I. Morphology and cartilage matrix production.* Connective tissue research, 1988. **18**(3): p. 205-222.
27. Goldring, M., et al., *Defining the roles of inflammatory and anabolic cytokines in cartilage metabolism.* Annals of the rheumatic diseases, 2008. **67**(Suppl 3): p. iii75-iii82.
28. Lotz, M., et al., *Cytokine regulation of chondrocyte functions.* The Journal of rheumatology. Supplement, 1995. **43**: p. 104.
29. Huber, M., S. Trattnig, and F. Lintner, *Anatomy, biochemistry, and physiology of articular cartilage.* Investigative radiology, 2000. **35**(10): p. 573.
30. Verzijl, N., et al., *Effect of collagen turnover on the accumulation of advanced glycation end products.* Journal of Biological Chemistry, 2000. **275**(50): p. 39027-39031.
31. Maroudas, A., et al., *Aggrecan turnover in human articular cartilage: use of aspartic acid racemization as a marker of molecular age.* Archives of biochemistry and biophysics, 1998. **350**(1): p. 61-71.
32. Mollenhauer, J., et al., *Role of anchorin CII, a 31,000-mol-wt membrane protein, in the interaction of chondrocytes with type II collagen.* The Journal of cell biology, 1984. **98**(4): p. 1572-1579.
33. Raya, J.G., et al., *Ultra high field diffusion tensor imaging of articular cartilage correlated with histology and scanning electron microscopy.* Magn Reson Mater Phy, 2011. **24**(4): p. 247-258.
34. WEISS, C., L. ROSENBERG, and A.J. HELFET, *An ultrastructural study of normal young adult human articular cartilage.* The Journal of Bone and Joint Surgery (American), 1968. **50**(4): p. 663-674.
35. Narayan, R., *Biomedical materials*. 2009: Springer.
36. Slowman, S.D. and K.D. Brandt, *Composition and glycosaminoglycan metabolism of articular cartilage from habitually loaded and habitually unloaded sites.* Arthritis & Rheumatism, 1986. **29**(1): p. 88-94.
37. Venn, M., *Variation of chemical composition with age in human femoral head cartilage.* Annals of the rheumatic diseases, 1978. **37**(2): p. 168-174.
38. Buckwalter, J.A., K.E. Kuettner, and E.J. Thonar, *Age-related changes in articular cartilage proteoglycans: electron microscopic studies.* J Orthop Res., 1985. **3(3):251-7.**
39. Buckwalter, J.A., P.J. Roughley, and L.C. Rosenberg, *Age-related changes in cartilage proteoglycans: quantitative electron microscopic studies.* Microsc Res Tech, 1994. **28**(5): p. 398-408.
40. Brown, M., et al., *Changes in sulfation patterns of chondroitin sulfate in equine articular cartilage and synovial fluid in response to aging and osteoarthritis.* American journal of veterinary research, 1998. **59**(6): p. 786.
41. Quinn, T.M., E.B. Hunziker, and H.J. Häuselmann, *Variation of cell and matrix morphologies in articular cartilage among locations in the adult human knee.* Osteoarthritis and Cartilage, 2005. **13**(8): p. 672-678.

42. Maroudas, A.I., *Balance between swelling pressure and collagen tension in normal and degenerate cartilage.* Nature, 1976. **260**(5554): p. 808-9.
43. Maroudas, A., et al., *Studies of hydration and swelling pressure in normal and osteoarthritic cartilage.* Biorheology, 1985. **22**(2): p. 159-69.
44. Xia, Y., *Magic-angle effect in magnetic resonance imaging of articular cartilage: a review.* Invest Radiol, 2000. **35**(10): p. 602-21.
45. Fernandes, J.C., J. Martel-Pelletier, and J.P. Pelletier, *The role of cytokines in osteoarthritis pathophysiology.* Biorheology, 2002. **39**(2): p. 237-246.
46. Krasnokutsky, S., J. Samuels, and S.B. Abramson, *Osteoarthritis in 2007.* BULLETIN-HOSPITAL FOR JOINT DISEASES NEW YORK, 2007. **65**(3): p. 222.
47. Amin, A.R., et al., *The expression and regulation of nitric oxide synthase in human osteoarthritis-affected chondrocytes: evidence for up-regulated neuronal nitric oxide synthase.* The Journal of experimental medicine, 1995. **182**(6): p. 2097-2102.
48. Hancock, C.M. and C. Riegger-Krugh, *Modulation of pain in osteoarthritis: the role of nitric oxide.* The clinical journal of pain, 2008. **24**(4): p. 353.
49. Myers, S., et al., *Prevalence of cartilage shards in synovium and their association with synovitis in patients with early and endstage osteoarthritis.* The Journal of rheumatology, 1992. **19**(8): p. 1247.
50. Horton, W., P. Bennion, and L. Yang, *Cellular, molecular, and matrix changes in cartilage during aging and osteoarthritis.* Journal of Musculoskeletal and Neuronal Interactions, 2006. **6**(4): p. 379.
51. Arden, N. and M.C. Nevitt, *Osteoarthritis: epidemiology.* Best Practice & Research Clinical Rheumatology, 2006. **20**(1): p. 3-25.
52. Oliveria, S.A., et al., *Estrogen replacement therapy and the development of osteoarthritis.* Epidemiology, 1996: p. 415-419.
53. Altman, R., et al., *Development of criteria for the classification and reporting of osteoarthritis. classification of osteoarthritis of the knee. Diagnostic and therapeutic criteria committee of the American Rheumatism Association.* Arthritis Rheum, 1986. **29**: p. 1039-1049.
54. Manek, N.J. and N.E. Lane, *Osteoarthritis: current concepts in diagnosis and management.* Am Fam Physician, 2000. **61**(6): p. 1795-804.
55. Kellgren, J. and J. Lawrence, *Radiological assessment of osteo-arthrosis.* Annals of the rheumatic diseases, 1957. **16**(4): p. 494-502.
56. Duncan, R.C., et al., *Prevalence of radiographic osteoarthritis -- It all depends on your point of view.* Rheumatology, 2006. **45**(6): p. 757-760.
57. Byers, P., C. Contepomi, and T. Farkas, *A post mortem study of the hip joint. Including the prevalence of the features of the right side.* Annals of the rheumatic diseases, 1970. **29**(1): p. 15-31.
58. Jordan, K., et al., *EULAR Recommendations 2003: an evidence based approach to the management of knee osteoarthritis: Report of a Task Force of the Standing Committee for International Clinical Studies Including Therapeutic Trials (ESCISIT).* Annals of the rheumatic diseases, 2003. **62**(12): p. 1145-1155.
59. Conaghan, P.G., J. Dickson, and R.L. Grant, *Care and management of osteoarthritis in adults: summary of NICE guidance.* Bmj, 2008. **336**(7642): p. 502-503.
60. Zhang, W., et al., *OARSI recommendations for the management of hip and knee osteoarthritis, Part II: OARSI evidence-based, expert consensus guidelines.* Osteoarthritis and Cartilage, 2008. **16**(2): p. 137-162.
61. Gamble, R., et al., *Recommendations for the medical management of osteoarthritis of the hip and knee.* Arthritis & Rheumatism, 2000. **43**(9): p. 1905-1915.

62. Maroudas, A., H. Muir, and J. Wingham, *The correlation of fixed negative charge with glycosaminoglycan content of human articular cartilage.* Biochim Biophys Acta, 1969. **177**(3): p. 492-500.
63. Gray, M.L. and D. Burstein, *Cartilage Matrix Assessment Using dGEMRIC*, in *Cartilage Imaging*. 2011, Springer. p. 171-183.
64. Li, X., *MR T1ρ Relaxation Time Quantification in Cartilage*, in *Cartilage Imaging*. 2011, Springer. p. 159-169.
65. Bashir, A., M.L. Gray, and D. Burstein, *Gd-DTPA2- as a measure of cartilage degradation.* Magn Reson Med, 1996. **36**(5): p. 665-673.
66. Burstein, D., et al., *Protocol issues for delayed Gd(DTPA)(2-)-enhanced MRI (dGEMRIC) for clinical evaluation of articular cartilage.* Magn Reson Med, 2001. **45**(1): p. 36-41.
67. Redfield, A.G., *Nuclear magnetic resonance saturation and rotary saturation in solids.* Physical Review, 1955. **98**(6): p. 1787.
68. Bull, T., *Relaxation in the rotating frame in liquids.* Progress in nuclear magnetic resonance spectroscopy, 1992. **24**(5): p. 377-410.
69. Li, X., et al., *In vivo 3T spiral imaging based multi-slice T(1rho) mapping of knee cartilage in osteoarthritis.* Magn Reson Med, 2005. **54**(4): p. 929-36.
70. Regatte, R.R., et al., *3D-T1rho-relaxation mapping of articular cartilage: in vivo assessment of early degenerative changes in symptomatic osteoarthritic subjects.* Academic radiology, 2004. **11**(7): p. 741.
71. Duvvuri, U., et al., *Human knee: in vivo T1(rho)-weighted MR imaging at 1.5 T--preliminary experience.* Radiology, 2001. **220**(3): p. 822-6.
72. Baum, T., T.M. Link, and B.J. Dardzinski, *MR T2 Relaxation Time Measurements for Cartilage and Menisci*, in *Cartilage Imaging*. 2011, Springer. p. 145-158.
73. Dunn, T.C., et al., *T2 relaxation time of cartilage at MR imaging: Comparison with severity of knee osteoarthritis.* Radiology, 2004. **232**(2): p. 592-8.
74. Li, X., et al., *In vivo $T_{1\rho}$ and T_2 mapping of articular cartilage in osteoarthritis of the knee using 3T MRI.* Osteoarthritis and Cartilage, 2007. **15**(7): p. 789-797.
75. Stahl, R., et al., *T1rho, T2 and focal knee cartilage abnormalities in physically active and sedentary healthy subjects versus early OA patients—a 3.0-Tesla MRI study.* European radiology, 2009. **19**(1): p. 132-143.
76. Yao, W., et al., *The application of T1 and T2 relaxation time and magnetization transfer ratios to the early diagnosis of patellar cartilage osteoarthritis.* Skeletal Radiol, 2009. **38**(11): p. 1055-1062.
77. Deng, X., et al., *Diffusion tensor imaging of native and degenerated human articular cartilage.* Magn Reson Imag, 2007. **25**(2): p. 168-171.
78. Wluka, A.E., et al., *The determinants of change in tibial cartilage volume in osteoarthritic knees.* Arthritis & Rheumatism, 2002. **46**(8): p. 2065-2072.
79. Cicuttini, F., et al., *The determinants of change in patella cartilage volume in osteoarthritic knees.* J Rheumatol, 2002. **29**(12): p. 2615-9.
80. Cicuttini, F., et al., *Rate of cartilage loss at two years predicts subsequent total knee arthroplasty: a prospective study.* Ann Rheum Dis, 2004. **63**(9): p. 1124-7.
81. Eckstein, F. and W. Wirth, *Quantitative cartilage imaging in knee osteoarthritis.* Arthritis, 2010. **2011**.
82. Fick, A., *Ueber diffusion.* Annalen der Physik, 1855. **170**(1): p. 59-86.
83. Johansen-Berg, H. and T.E. Behrens, *Diffusion MRI: From quantitative measurement to in-vivo neuroanatomy*. 2009: Academic Press.

84. Le Bihan, D., et al., *MR imaging of intravoxel incoherent motions: application to diffusion and perfusion in neurologic disorders.* Radiology, 1986. **161**(2): p. 401.
85. Mintorovitch, J., et al., *Comparison of diffusion-and T2-weighted MRI for the early detection of cerebral ischemia and reperfusion in rats.* Magnetic resonance in medicine, 1991. **18**(1): p. 39-50.
86. Baur, A., et al., *Diffusion-weighted MR imaging of bone marrow: differentiation of benign versus pathologic compression fractures.* Radiology, 1998. **207**(2): p. 349-356.
87. Raya, J.G., et al., *Techniques for diffusion-weighted imaging of bone marrow.* Eur J Radiol, 2005. **55**(1): p. 64-73.
88. Raya, J., et al., *Methods and applications of diffusion imaging of vertebral bone marrow.* J Magn Reson Imaging, 2006. **24**(6): p. 1207-20.
89. Raya, J.G., et al., *Feasibility of a RARE-based sequence for quantitative diffusion-weighted MRI of the spine.* Eur Radiol, 2007. **17**(11): p. 2872-9.
90. Stejskal, E.O. and J. Tanner, *Spin diffusion measurements: Spin echoes in the presence of a time-dependent field gradient.* The journal of chemical physics, 1965. **42**: p. 288.
91. Reinges, M.H., et al., *Imaging of postthalamic visual fiber tracts by anisotropic diffusion weighted MRI and diffusion tensor imaging: principles and applications.* European journal of radiology, 2004. **49**(2): p. 91-104.
92. Le Bihan, D., et al., *Diffusion tensor imaging: concepts and applications.* J Magn Reson Imaging, 2001. **13**(4): p. 534-46.
93. Maroudas, A., *Physicochemical properties of cartilage in the light of ion exchange theory.* Biophysical journal, 1968. **8**(5): p. 575-595.
94. Maroudas, A. and M. Venn, *Chemical composition and swelling of normal and osteoarthrotic femoral head cartilage. II. Swelling.* Ann Rheum Dis, 1977. **36**(5): p. 399-406.
95. Mlynarik, V., et al., *Investigation of apparent diffusion constant as an indicator of early degenerative disease in articular cartilage.* J Magn Reson Imaging, 2003. **17**(4): p. 440-4.
96. Xia, Y., et al., *Self-diffusion monitors degraded cartilage.* Arch Biochem Biophys, 1995. **323**(2): p. 323-8.
97. Burstein, D., et al., *Diffusion of small solutes in cartilage as measured by nuclear magnetic resonance (NMR) spectroscopy and imaging.* J Orthop Res, 1993. **11**(4): p. 465-478.
98. Mlynarik, V., et al., *Investigation of laminar appearance of articular cartilage by means of magnetic resonance microscopy.* Magn Reson Imaging, 1996. **14**(4): p. 435-42.
99. de Visser, S.K., et al., *Anisotropy of collagen fibre alignment in bovine cartilage: comparison of polarised light microscopy and spatially resolved diffusion-tensor measurements.* Osteoarthritis Cartilage, 2008. **16**(6): p. 689-697.
100. Feldman, F., *Special Scientific Papers ISS 2008.* Skeletal Radiol, 2008. **37**: p. 955-962.
101. Raya, J.G., et al., *Diffusion-Tensor Imaging of Human Articular Cartilage Specimens with Early Signs of Cartilage Damage.* Radiology, 2013. **266**(3): p. 831-841.
102. Raya, J.G., et al., *In vivo diffusion tensor imaging (DTI) of articular cartilage of healthy and osteoarthritis (OA) subjects with coverage of all cartilage plates.* 20th annual meeting and exhibition of the International Society of Magnetic Resonance in the Medicine2012; Mealbourne, Victoria, Australia 2012.
103. Block, K.T., *Advanced Methods for Radial Data Sampling in Magnetic Resonance Imaging*. 2008, Niedersächsische Staats-und Universitätsbibliothek Göttingen.
104. Haacke, E.M., et al., *Magnetic resonance imaging: physical principles and sequence design*. Vol. 82. 1999: Wiley-Liss New York:.
105. Juchem, C., et al., *Magnetic field modeling with a set of individual localized coils.* Journal of Magnetic Resonance, 2010. **204**(2): p. 281-289.

106. Bernstein, M.A., K.F. King, and X.J. Zhou, *Handbook of MRI pulse sequences*. 2004: Academic Press.
107. Pauly, J., *Non-cartesian reconstruction.* URL: http://www.stanford. edu/class/ee369c/notes/non cart rec, 2007. **7**.
108. O'sullivan, J., *A fast sinc function gridding algorithm for Fourier inversion in computer tomography.* Medical Imaging, IEEE Transactions on, 1985. **4**(4): p. 200-207.
109. Jackson, J.I., et al., *Selection of a convolution function for Fourier inversion using gridding [computerised tomography application].* Medical Imaging, IEEE Transactions on, 1991. **10**(3): p. 473-478.
110. Block, K.T., M. Uecker, and J. Frahm, *Undersampled radial MRI with multiple coils. Iterative image reconstruction using a total variation constraint.* Magnetic resonance in medicine, 2007. **57**(6): p. 1086-1098.
111. Rudin, L.I., S. Osher, and E. Fatemi, *Nonlinear total variation based noise removal algorithms.* Physica D: Nonlinear Phenomena, 1992. **60**(1): p. 259-268.
112. Skare, S., et al., *Condition number as a measure of noise performance of diffusion tensor data acquisition schemes with MRI.* J Magn Reson, 2000. **147**: p. 340-352.
113. Jung, H., et al., *Radial k-t FOCUSS for high-resolution cardiac cine MRI.* Magnetic resonance in medicine, 2010. **63**(1): p. 68-78.
114. Le Bihan, D., et al., *Artifacts and pitfalls in diffusion MRI.* Journal of Magnetic Resonance Imaging, 2006. **24**(3): p. 478-488.
115. König, L., M. Groher, and A. Keil, *Semi-automatic Segmentation of the Patellar Cartilage in MRI.* Bildverarbeitung für die Medizin, 2007. **17**: p. 404-408.
116. Dietrich, O. *Diffusion Coefficients of Water*. 2002; Available from: http://dtrx.de/od/diff/.
117. Raya, J.G., et al. *In vivo DTI of articular cartialge at 3T with a spin echo radial diffusion tensor imaging (RAISED) sequence*. Proceedings of the 21st meeting of the International Society of Magnetic Resonance in the Medicine (ISMRM). 2013. Salt Lake City, UT, USA.

Statement of Authentication

I certify that all materials presented in this thesis are of my own creation, and that any work adopted from other sources is duly cited and referenced as such. This thesis has not been accepted for any degree and is not concurrently submitted for a degree at any other institution.

Oelixdorf, May 10th, 2013

B. Sc. Eike Susann Dettmann